UC Santa Cruz

UC Santa Cruz Previously Published Works

Title

In situ X-ray and IR probes relevant to Earth science at the Advanced Light Source at Lawrence Berkeley Laboratory

Permalink

https://escholarship.org/uc/item/4tz5r8nq

Journal

Physics and Chemistry of Minerals, 51(2)

ISSN

0342-1791

Authors

Kunz, Martin

Armstrong, Katherine

Barnard, Harold

et al.

Publication Date

2024-06-01

DOI

10.1007/s00269-024-01278-5

Copyright Information

This work is made available under the terms of a Creative Commons Attribution License, available at https://creativecommons.org/licenses/by/4.0/

Peer reviewed

eScholarship.org Powered by the California Digital Library
University of California

Physics and Chemistry of Minerals (2024) 51:15
https://doi.org/10.1007/s00269-024-01278-5

ORIGINAL PAPER

In situ X-ray and IR probes relevant to Earth science at the Advanced Light Source at Lawrence Berkeley Laboratory

Martin Kunz[1] · Katherine Armstrong[1,2] · Harold Barnard[1] · Hans A. Bechtel[1] · Samantha C. Couper[3] · Bora Kalkan[1,2] · Harry Lisabeth[4] · Alastair A. MacDowell[1] · Lowell Miyagi[3] · Dilworth Y. Parkinson[1] · Nobumichi Tamura[1] · Quentin Williams[2]

Received: 14 July 2023 / Accepted: 20 March 2024 / Published online: 28 April 2024
This is a U.S. Government work and not under copyright protection in the US; foreign copyright protection may apply 2024

Abstract
Access to synchrotron X-ray facilities has become an important aspect for many disciplines in experimental Earth science. This is especially important for studies that rely on probing samples in situ under natural conditions different from the ones found at the surface of the Earth. The non-ambient condition Earth science program at the Advanced Light Source (ALS), Lawrence Berkeley National Laboratory, offers a variety of tools utilizing the infra-red and hard X-ray spectrum that allow Earth scientists to probe Earth and environmental materials at variable conditions of pressure, stress, temperature, atmospheric composition, and humidity. These facilities are important tools for the user community in that they offer not only considerable capacity (non-ambient condition diffraction) but also complementary (IR spectroscopy, microtomography), and in some cases unique (Laue microdiffraction) instruments. The availability of the ALS' in situ probes to the Earth science community grows especially critical during the ongoing dark time of the Advanced Photon Source in Chicago, which massively reduces available in situ synchrotron user time in North America.

Keywords Synchrotron · In situ X-ray diffraction · In situ IR spectroscopy · In situ X-ray tomography

Introduction

Earth scientists have been at the forefront of utilizing synchrotron radiation for their research from the earliest days of user-facility synchrotron light sources (Calas et al. 1984; Häusermann 1992; Hemley et al. 1998; Sutton et al. 1988; Yagi 1988). This community became pioneering users and drivers of synchrotron development due to their collective need for analysis techniques that could resolve very small sample volumes with high brightness, a wide wavelength spectrum, and a high photon flux. Over time, the number and complexity of synchrotron techniques that found applications in Earth and environmental sciences has expanded to include X-ray absorption, emission and resonance spectroscopy, as well as sophisticated time-resolved scattering and diffraction techniques (Anzellini et al. 2013; Cnudde and Boone 2013; Fenter et al. 2018; Kupenko et al. 2012; Lavina et al. 2014; Quartieri 2015). One common thread in these efforts, regardless of the technique applied, was and remains the frequent need to combine the X-ray probe with conditions that are different to those on the Earth's surface. Specifically, many geologic research questions require high pressures and stress/strain (to simulate the planet's interior), extreme temperatures (planet's interior, hydrothermal environments, volcanology, surface of extraterrestrial planetary bodies), variable atmospheric compositions and humidity levels (environmental science, hydrology), and combinations of these. Ancillary equipment that can contain a sample under controlled non-ambient conditions must be transparent to the electromagnetic radiation acting as a probe; light in the infrared (IR) and hard X-ray ranges tends to be the most amenable. It is mainly for this reason that the bulk of

✉ Martin Kunz
mkunz@lbl.gov

[1] Advanced Light Source, Lawrence Berkeley Lab, 1 Cyclotron Rd, Berkeley, CA 94720, USA

[2] Earth and Planetary Sciences, UC Santa Cruz, 1156 High Street, Santa Cruz, CA 95064, USA

[3] Geology and Geophysics, 115 S 1460 E, Salt Lake City, UT 84112-0102, USA

[4] Earth and Environmental Sciences, Lawrence Berkeley Lab, 1 Cyclotron Rd, Berkeley, CA 94720, USA

in situ synchrotron geoscience research relies on techniques that employ IR and/or X-rays with energies above ~5 keV.

The US Department of Energy operates synchrotron user facilities that offer a variety of instruments to the Earth science community at Brookhaven National Lab (National Synchrotron Light Source, NSLS-II), Argonne National Lab (Advanced Photon Source, APS), SLAC National Accelerator Lab (Linac Coherent Light Source, LCLS and Stanford Synchrotron Radiation Lightsource, SSRL) and Lawrence Berkeley Lab (Advanced Light Source, ALS); the Cornell High Energy Synchrotron Source (CHESS) is operated by the National Science Foundation. Recently, Bommannavar et al. (2022), Sutton et al. (2022) and Zhang et al. (2022) nicely summarized capabilities at the APS that are helping to confront many of the current pressing problems in Earth science, and Laasch et al. (2022) documented capabilities at NSLS-II relevant to Earth science research.

The APS of Argonne National Lab and the ALS at Lawrence Berkeley Lab are both scheduled to undergo major accelerator upgrades that will transform the aging electron storage rings towards an 'ultimate storage ring', capable of emitting nearly fully coherent X-rays at their respective energies. The APS was first to undergo a 1–2 year long dark time to implement this upgrade, beginning in the spring of 2023. This leaves a temporary but significant gap in domestic synchrotron capabilities in the US. While many of Lawrence Berkeley Lab's ALS Earth and environmental science-oriented beamlines are distinct from the APS suite, the ALS also hosts some instruments that offer similar capabilities. The purpose of this paper is to introduce (or remind) the Earth science community of the synchrotron IR and hard X-ray capabilities at the ALS in Berkeley. Experiments under non-ambient conditions are conducted on its IR beamlines (1.4, 2.4 and 5.4) and on three of its hard X-ray superbend beamlines, namely 8.3.2 (X-ray micro-tomography), 12.2.2 (X-ray diffraction under non-ambient conditions) and 12.3.2 (Laue X-ray microdiffraction). Here we present an overview of the in situ non-ambient condition experimental capabilities that these beamlines offer to the Earth science user community, with a special emphasis on aspects not previously published elsewhere.

Infrared spectroscopy: beamlines 1.4, 2.4 and 5.4

Although the ALS is optimized to produce X-rays, synchrotron bend magnet radiation is broadband and continues to be a bright source into the infrared region. This non-ionizing infrared light can be exploited to probe low-energy electronic excitations and molecular vibrations in a variety of materials using Fourier-transform infrared (FTIR) spectroscopy. The ALS has three IR beamlines, namely Beamlines 1.4, 2.4, and 5.4, that take advantage of the source characteristics to perform IR micro- and nano-spectroscopy experiments on small and complex heterogeneous materials, with applications ranging from the deep earth to deep space and everywhere in between.

In an IR micro-spectroscopy experiment (Fig. 1a), broadband synchrotron IR light is first passed through a symmetric Michelson interferometer and is then focused onto a sample with reflective Schwarzschild objectives. The diffraction-limited spot size is approximately 2–10 μm for typical mid-infrared wavelengths (Dumas et al. 2020). After interacting with the sample, the reflected or transmitted IR light is detected by a suitable infrared detector (typically an HgCdTe detector) and the resulting interference signal is Fourier transformed to obtain an IR spectrum. Samples are routinely raster scanned to obtain 3D hyperspectral images spanning the IR spectral range. A choice of infrared objectives allows variable working distances up to 8–15 mm. This facilitates the use of a variety of devices that enable sample analysis over a wide range of ambient and non-ambient conditions, including microfluidic cells for studying biomolecules and organisms in hydrated environments (Hazen et al. 2010; Holman et al. 2010; Loutherback et al. 2016); diamond anvil cells (DACs) and inclusions in naturally occurring diamonds for investigating materials under high pressure (Chen et al. 2020; Nisr et al. 2020; Tschauner et al. 2018, 2021); cryostats for low and high temperature measurements; as well as soils (Bouskill et al. 2016; Keiluweit et al. 2015) and extraterrestrial materials (Ishii et al. 2018; Sandford et al. 2006; Westphal et al. 2014).

Figure 2 illustrates using IR spectroscopy to investigate subsurface biofilms obtained from cold, sulfidic springs at the Sippenauer Moor (Probst et al. 2013). Usually archaea are found in moderate and cold environments as minority members of a much larger microbial community. Archaea in biofilms from the Sippenauer Moor, however, are the dominant species in the symbiotic "string of pearls" community, in which SM1 Euryarchaeon fill the "pearls" and the filamentous bacteria cover the pearl surfaces and form strings between them. Although the two types of microbes were assumed to be syntrophic, the biochemical details were unknown. Here, IR imaging was able to map the locations of the bacteria and archaea and identify the chemical relationships between them, showing unambiguously the sulfate-reducing metabolic activity of the bacteria and lack of such activity in the archaeal cells.

In a synchrotron IR nano-spectroscopy experiment (Fig. 1b), broadband synchrotron IR light is coupled into an asymmetric Michelson interferometer, where half of the light is focused onto an oscillating atomic force microscope (AFM) tip operating in close proximity to the sample surface (Bechtel et al. 2020). The resulting scattered light is collected and recombined with the other half of the

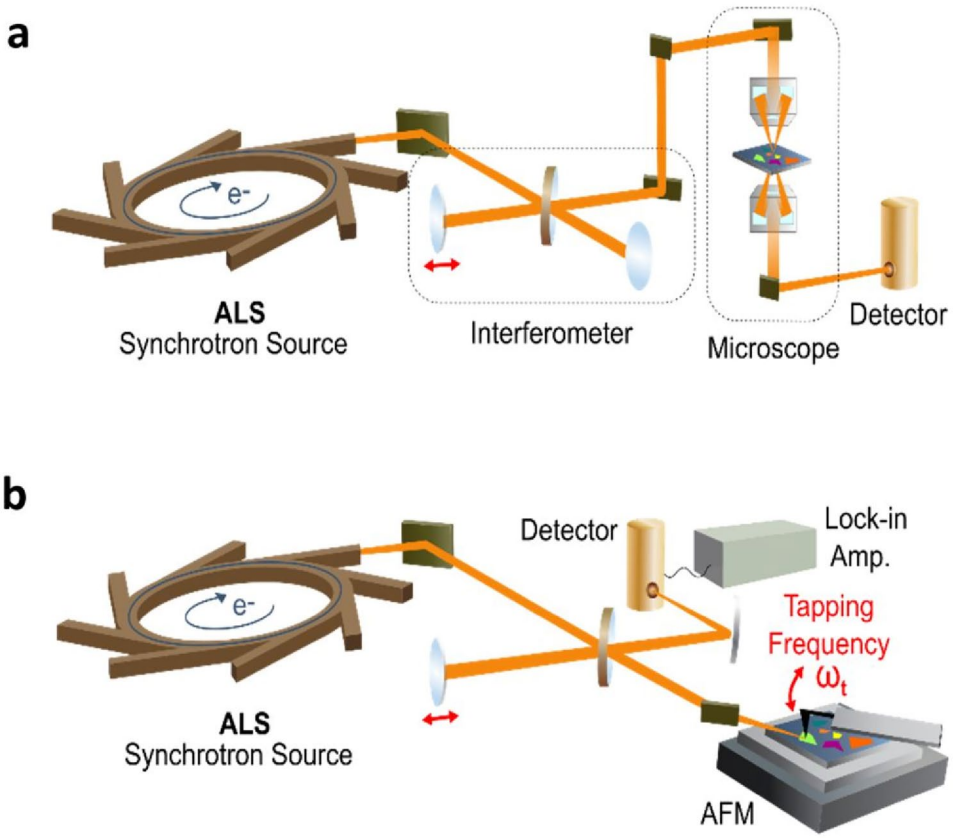

Fig. 1 **a** Schematic of an IR microscopy experiment in transmission geometry. **b** Schematic of an IR nano-spectroscopy measurement

input light, which has been reflected off a moving mirror. The resulting interference between the tip-scattered light and the reference light is measured with an IR detector and demodulated at harmonics of the tip-tapping frequency (ω_t) to remove background scattering before being Fourier-transformed to yield an IR spectrum with information about the real (reflection) and imaginary (absorption) components of the dielectric constant of the sample. In this case, the AFM tip localizes the electric field and provides a tip-limited spatial resolution of <20 nm, enabling chemical imaging at the nanoscale, nearly three orders of magnitude smaller than the diffraction limit. Sample requirements for IR nano-spectroscopy are stricter than for IR micro-spectroscopy measurements, with a major requirement being that the samples are sufficiently flat for AFM measurements. Sample height variations of <500 nm are preferred, but up to 2 µm height variations can be accommodated. Nanoscale heterogeneities can be explored with this technique, as recently demonstrated in naturally occurring shale (Hao et al. 2018); calcium carbonate polymorphs (Bechtel et al. 2014); and meteorite mineralogy (Young et al. 2022). The requirement for the AFM tip to be in close proximity to the sample limits the types of non-ambient conditions that can be accessed using this technique, although variable temperature measurements from room temperature up to 375 K are possible, as well as limited measurements in liquids with liquid cell designs (Lu et al. 2019; Zhao et al. 2022).

Figure 3 shows synchrotron IR nano-spectroscopy measurements of a small piece of shale (Hao et al. 2018). Shale is the most common sedimentary rock and is composed of mineral particles mixed with variable quantities of organic matter. This mixture forms a nanoporous network that can trap and store fluids, and affects a variety of applications, including hydraulic fracturing, enhanced geothermal heating, carbon sequestration, and water storage. As shown in the figure, the nano-spectroscopy measurements reveal the heterogeneity of the shale and are able to identify different mineral components and organic-rich areas at the nanoscale. These results have been combined with lower spatial resolution IR micro-spectroscopy measurements covering larger fields of view to perform cross-scale molecular analyses that reveal greater detail across nanopore and micrograin scales.

X-ray micro-tomography: beamline 8.3.2

Beamline 8.3.2 was recommissioned with a new endstation in 2007. It is situated on a superconducting bend magnet and the electron source (of size 94 × 17 µm FWHM) sees a field of 4.37 T, yielding a critical energy of 11.5 keV. The source-to-sample distance is 20 m; with no focusing optics on the

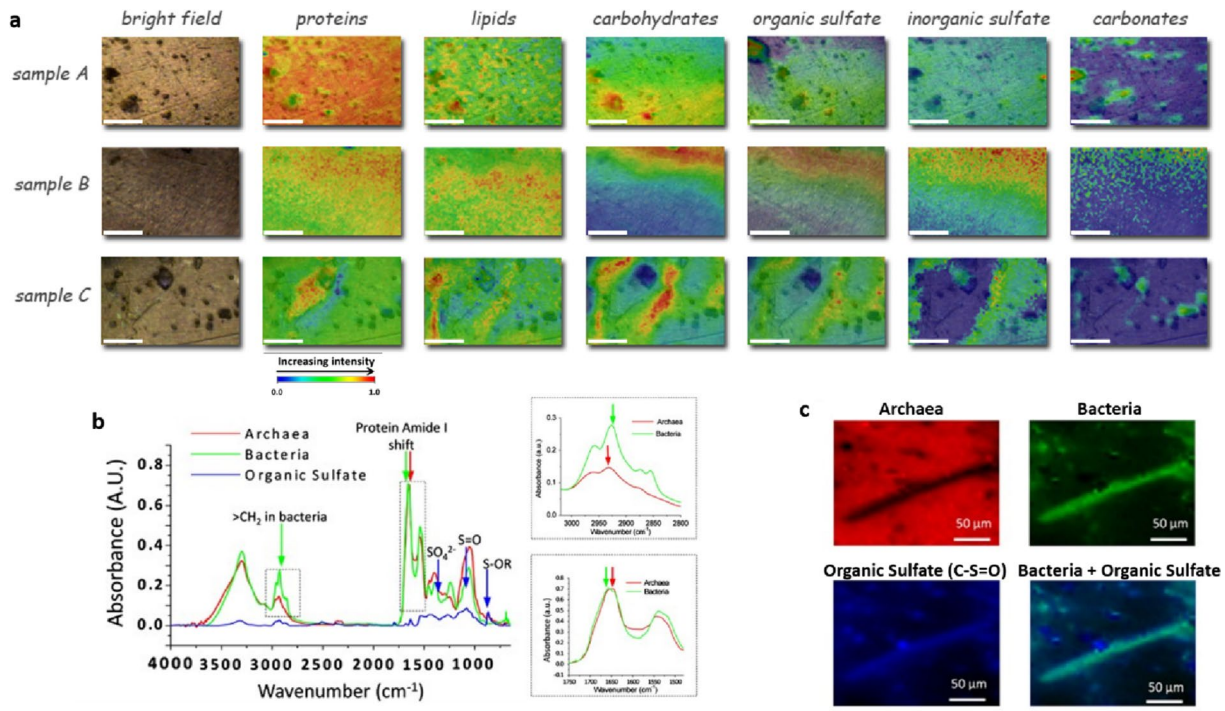

Fig. 2 Synchrotron IR micro-spectroscopy images and spectra of bacteria in an archaea-dominated biofilm. **a** Heat map from univariate analysis showing the distribution of key biomolecules and sulfur/carbon biogeochemical cycling products in three different biofilms (A, B, C) from a sulfidic spring. Scale bars = 50 µm. **b** Spectra of three components extracted from multivariate analysis: archaea (red), bacteria (green), and organic sulfate features (blue), with arrows pinpointing the spectral markers used in the analysis. Panel insets are zoomed in to highlight the spectral region of lipids and proteins, which are an important region for the distinction of bacteria and archaea because of their different membrane and protein composition. **c** Relative concentration images of archaea, bacteria, and organic sulfate (C–S=O) recovered by multivariate analysis. Merging the relative bacterial concentration image (green) with the organic sulfate distribution map (blue) reveals the co-localization of bacteria and organic sulfate. Scale bars = 50 µm. Figure adapted from Probst et al. (2013)

beamline the beam size at the sample is ~40 mm × 4.6 mm (2 × 0.23 mrad @ 20 m). The beamline can currently be operated in either white light mode, in which no optics are used in the beam, or in monochromatic mode, in which a multilayer monochromator (W/B_4C, d = 2 nm, 1% bandpass) is used over an energy range of approximately 8–40 keV. For many Earth science experiments, white light is used both because it allows higher flux and thus higher time resolution, and because it allows access to X-ray energies higher than the range of the monochromator, which are often necessary to penetrate geologic samples as well as associated sample environments.

The sample is mounted on an air-bearing rotation stage that in turn is mounted over a hole in the optical support table. This arrangement allows the sample mounting system to be translated over a long distance, allowing tall samples up to 60 cm in size to be imaged. Detection is performed using thin scintillators (i.e., 50 µm thick LuAG:Ce), imaging these with optical lenses onto a CMOS detector (currently a PCO.edge). The detection system has multiple resolution and configuration options. An Optique Peter lens system is used with lenses in-line when imaging in monochromatic mode. Home-built lens systems with lenses out of the X-ray path are employed in white light mode. Lenses span 1× to 20×, corresponding to pixel sizes of 6.5 to 0.325 µm.

A tomographic scan is carried out by rotating a sample through 180° and collecting hundreds to thousands of images. Exposure times are typically a few milliseconds in white light mode, and a few hundred milliseconds in monochromatic mode. Scan times for a full tomographic scan of one field of view thus range from under a minute to 10 min, depending on the requirements of collection time, spatial resolution, and image quality. An advanced data pipeline has been developed, whereby a data orchestration system automatically moves data as it is collected to the National Energy Research Science Computing Center (NERSC), the high-performance computing system at Berkeley Lab. Users have access to a web-based system based on Jupyter notebooks for data processing, which also runs at NERSC, with templates and processing routines that allow them to run tomographic reconstruction using TomoPy, ASTRA, and SVMBIR. Users can download raw and processed data from NERSC using globus.org or other tools available at NERSC.

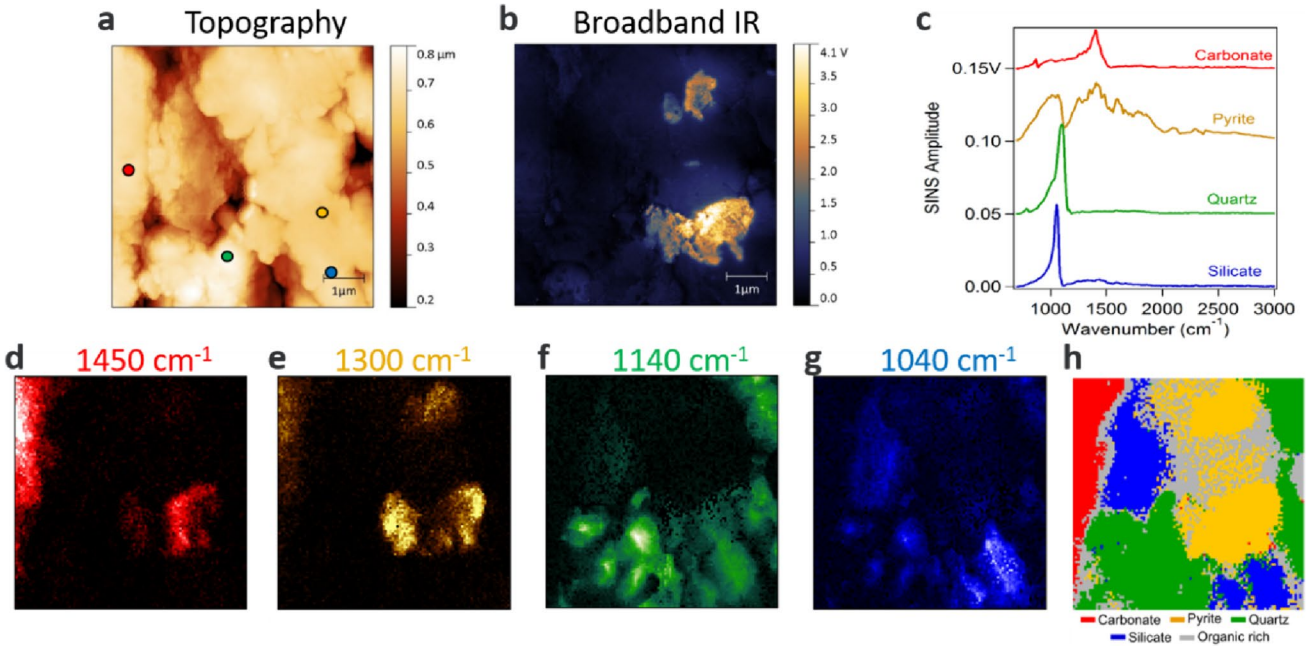

Fig. 3 Synchrotron IR nano-spectroscopy measurements of shale. Simultaneously collected **a** topography and **b** broadband IR amplitude images revealing contrast between the various components of the shale, with highly reflecting components (metals) appearing brighter. **c** IR nano-spectroscopy measurements of the different components in shale, identified by the dots in panel **a**. **d**–**g** IR heat maps of a single frequency, representative of the different colored components in **c**. **h** principle component analysis clustering of the different shale components based on the entire spectral measurements. Adapted from Hao et al. (2018)

The sample environments available to users at 8.3.2 include capabilities for heating, cooling, and mechanical testing. There are also sample environments developed by users from the LBNL Earth and Environmental Sciences Area that allow for flowing gas and liquids through samples that are at pressure. Two vessels have been built for use at slightly elevated (20–80 °C) and high-temperature experiments (up to 400 °C). Both vessels are capable of triaxial stress states with confining pressures up to 25 MPa and axial stress up to 40 MPa. The lower temperature vessel is optimized for studying multiphase (Garing et al. 2017a, b; Zuo et al. 2017) and reactive flow (Deng et al. 2016, 2017; Voltolini and Ajo-Franklin 2019) in porous materials, while the higher temperature cell is used for thermally activated processes such as creep (Voltolini 2021) and pyrolysis (Voltolini et al. 2019).

Nano-tomography: beamline 11.3.1

As a complement to the micro-tomography program, beamline 11.3.1 at the Advanced Light Source is a tender/hard (6–17 keV) X-ray bend magnet beamline that was recently repurposed with a new full-field, nanoscale transmission X-ray microscope. The microscope is designed to image composite and porous materials that have sub-micrometer structure and compositional heterogeneity that governs materials' performance and geologic behavior. The theoretical and achieved resolutions are 55 and <100 nm, respectively. The microscope is used in tandem with a <25 nm eccentricity rotation stage for high-resolution volume imaging using nanoscale computed tomography. The system also features a novel quadrupole illumination condenser for the illumination of an ~100 µm spot of interest on the sample, followed by a phase-type zone plate magnifying objective of ~52 µm field-of-view and a phase detection ring. The zone plate serves as the system objective and magnifies the sample via projection onto an indirect X-ray detection system, consisting of a polished single crystal CsI (Tl) scintillator and a range of high-quality Plan Fluorite visible light objectives. The objectives project the final visible light image onto a water-cooled CMOS 2048 × 2048-pixel2 detector. Additional details of the system can be found in Nichols et al. (2022).

Mechanical-environmental cell

A mechanical loading device has been developed in parallel with the nano-tomography beamline in order to perform in situ mechanical testing with concurrent imaging. The apparatus consists of a single loading column supported by a c-frame (Fig. 4). Samples are fixed between two hollow, needle-shaped loading platens which are sealed to pipe fittings,

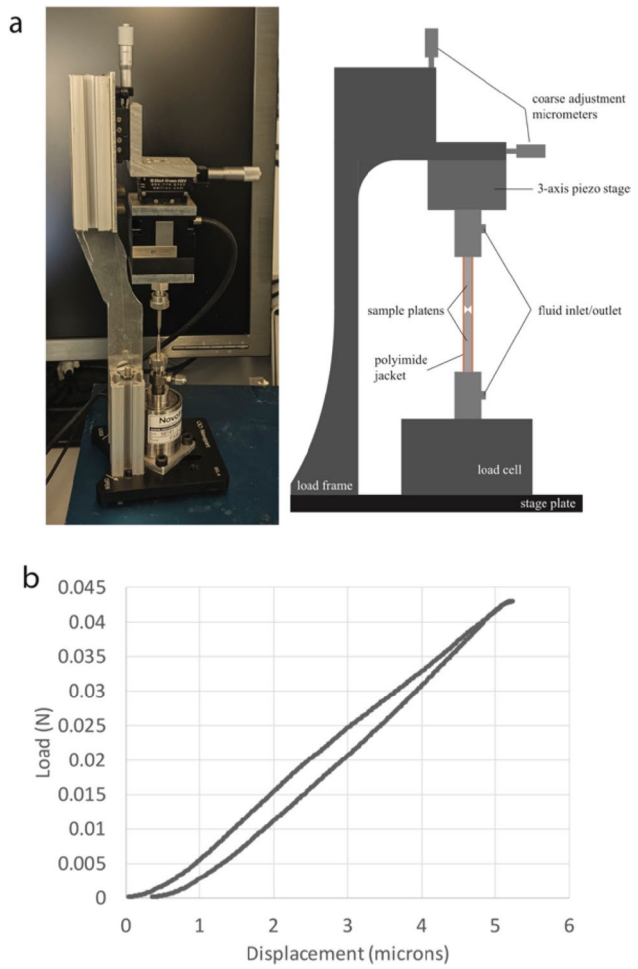

Fig. 4 Nanomechanical loading device. **a** A picture and schematic of the device and **b** example of mechanical data from a constant displacement rate deformation experiment on a single calcite grain

allowing fluid to flow within the annulus between the sample and a polyimide jacket. Force is measured using an integrated donut-style load cell with a linear range of 0–10 N. For a sample with a 40-micron circular cross-section, this amounts to an axial stress range of more than 8 GPa. Three micrometers arranged orthogonally allow for coarse positioning of the platens, while fine control is provided by a three-axis piezo-controlled stage (PI Nanocube). Each axis has a range of 120 microns and the piezoelectric crystal stacks are affixed with strain gauges to allow for closed-loop displacement control with a resolution of 0.2 nm. The stage is driven by a computer-integrated piezo controller (Physik Instumente E-727) that allows arbitrary loading paths and direct feedback from the integrated load cell. This apparatus is designed for contact-scale mechanics studies in the presence of chemically reactive fluids and is well suited for single grain as well as grain-grain experiments. An example of mechanical data from a constant displacement rate experiment on a single calcite grain is presented in Fig. 4b. This data can be used to characterize the static elastic properties of granular materials as well as the onset of microplasticity and the role of chemistry on the grain scale.

An example of the kind of scientific questions that can be addressed with micro-tomography (miroCT) at Beamline 8.3.2 is given by Voltolini and Ajo-Franklin (2020). In their work, in situ microCT was used to study the sealing of a single fracture in opalinus clay, a proposed nuclear waste repository material (Fig. 5). Opalinus clay (OPA) is a shale with 40–70 wt.% clay minerals (mostly non-swelling clays), 10–30 wt.% carbonates (mainly calcite, subordinate siderite, and ankerite), 10–30 wt.% quartz and accessory feldspars, pyrite, and organic matter. It has well documented self-sealing properties. For the experiment it was soaked in CO_2 saturated water. 4D X-ray microCT sections were collected as a function of confining pressure (up to 700 psi differential pressure). The experiment revealed the influence of different factors in the sealing of the fractured rocks. Hydration-induced swelling, microcracking, and mechanical weakening lead to closing of the asperity contacts. The development of the asperity contacts controls the development of localized choke points, which in turn control the hydraulic properties of the fracture and thus rock sample. Understanding the coupled mechanical and hydraulic properties of fine-grained, heterogeneous materials like shale are important not only for geologic storage, but for energy and water resources as well. In situ observation of the effect of stress on the geometry of a fracture at realistic reservoir conditions is essential to unravel these coupled processes.

X-ray powder and single-crystal diffraction: beamline 12.2.2

ALS Beamline 12.2.2 was originally designed as a dedicated high-pressure X-ray diffraction beamline focusing on laser-heated diamond anvil cells (LHDAC) and was built and commissioned in 2003–2004. The light for 12.2.2 is produced from the 5.29 T side field of a 6 T superconducting bending magnet yielding a critical energy of 12.7 keV. Its optical design is based on a 2-stage focusing system. The first stage is a vertically collimating mirror, a Kohzu monochromator with both a Si(111) double crystal monochromator ($E/\Delta E \sim 10{,}000$) and a multilayer double monochromator ($E/\Delta E \sim 120$) followed by a toroidal M2 mirror to yield the primary focus spot at End Station 1 (ES1). Further downstream, the beam can be refocused with demagnification using a set of Kirkpatrick–Baez (K–B) mirrors onto End Station 2 (ES2). Details of these optics are described in Kunz et al. (2005). The beamline offers two end-stations (ES1 and ES2), which can be operated alternately. ES1, positioned at the primary focus point of the beamline, is optimized for high-pressure single-crystal diffraction, while ES2 allows

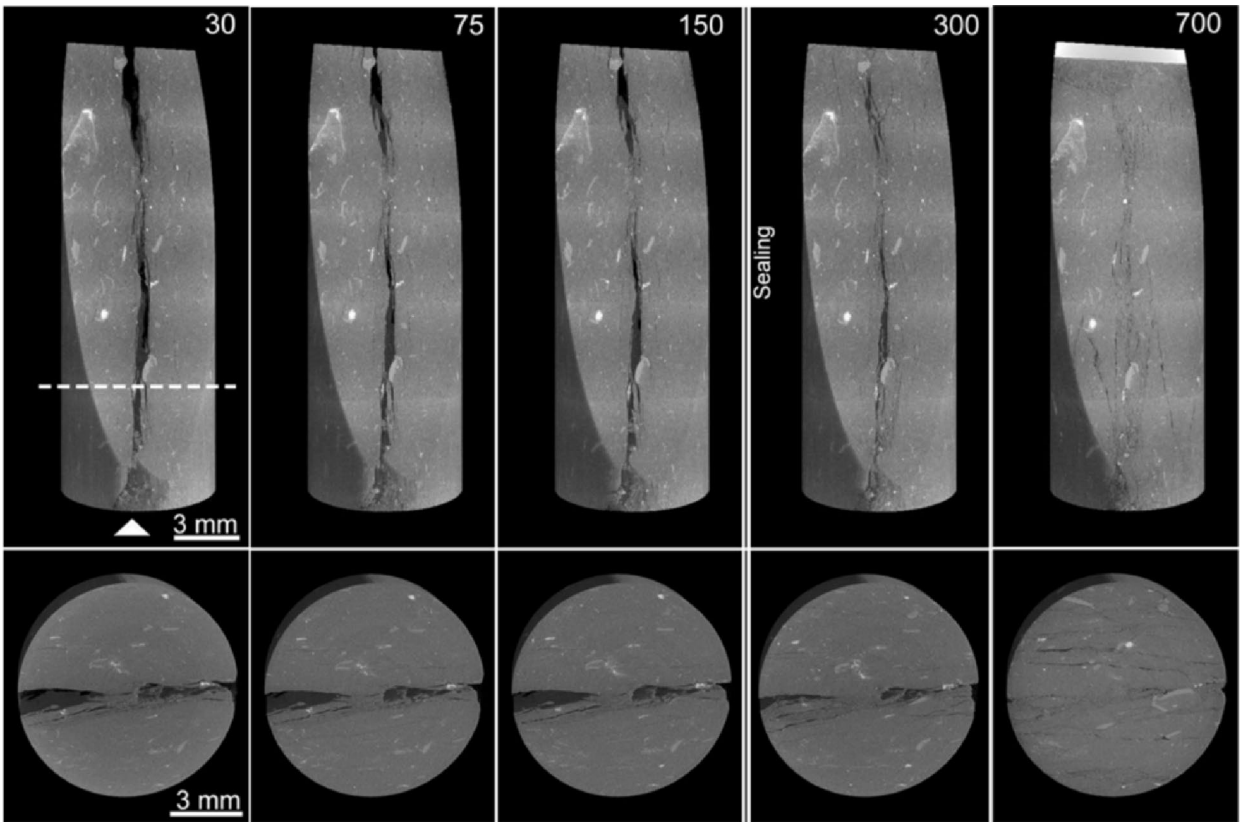

Fig. 5 Volume rendering of the OPA sample while increasing the confining pressure (volumes in figure are labeled with differential pressure values, in psi). The inlet is at the bottom (arrow in top left image). On the top row a subvertical section of the sample is shown. The bottom row displays a slice of sample (at the dashed line in the top left image) looking from the inlet direction. Figure adapted from Voltolini and Ajo-Franklin (2020)

for powder diffraction under various non-ambient conditions. Both ES1 and ES2 have recently installed new developments that are of interest for the Earth- and environmental science community. These are described below:

12.2.2: ES1

ES1 hosts a vertically-arranged STOE StadiVari X-ray diffractometer and a Dectris PILATUS3 × CdTe 300K detector (see Fig. 6) to perform high pressure X-ray single crystal diffraction measurements. The open Eulerian cradle of the diffractometer provides sufficient space to accommodate a set of motorized xyz stages for aligning and active sample position correction. This allows for accurate 4-circle goniometry of samples in holders such as diamond anvil cells weighing up to ~1 kg with a sphere of confusion below 10 microns. Two Aerotech stages move the entire setup transversely and vertically to bring the center of the goniometer onto the primary focus spot of the X-ray beam. A compact and custom-made Ta pinhole (X-ray aperture) with a round cross-section delivers the beam to the sample position with a FWHM spot size of 65 µm (horizontal) × 50 µm (vertical). A telescope equipped with a viewing camera at a 40° angle relative to the incoming beam helps with sample alignment and gives a field of view of nearly 1.2 × 1.2 mm.

Shutterless single-crystal X-ray diffraction measurements are performed at energies between 25 keV (0.4959 Å) and 33 keV (0.3757 Å). A typical exposure time of 0.5–2 s/° maximizes the intensities of the diffraction peaks without saturation. Beamline characteristics, such as sample distance and precise wavelength, are calibrated with a NIST standard single-crystal ruby sphere (SRM 1990) (Wong-Ng et al. 2001). Data is integrated using XAREA 1.76 (Stoe 2009). Integrated intensities are scaled and corrected for absorption (with the numerical absorption correction) using LANA (Koziskova et al. 2016) and X-RED32 (equivalent to the work of Coppens (1970)) packages embedded in XAREA.

12.2.2: ES2

The secondary focus spot of the beamline is created by a set of K–B mirrors that demagnify the primary focus spot in the horizontal and vertical by a factor of 2.19 and 6.14, respectively. ES2 was originally designed for double-sided

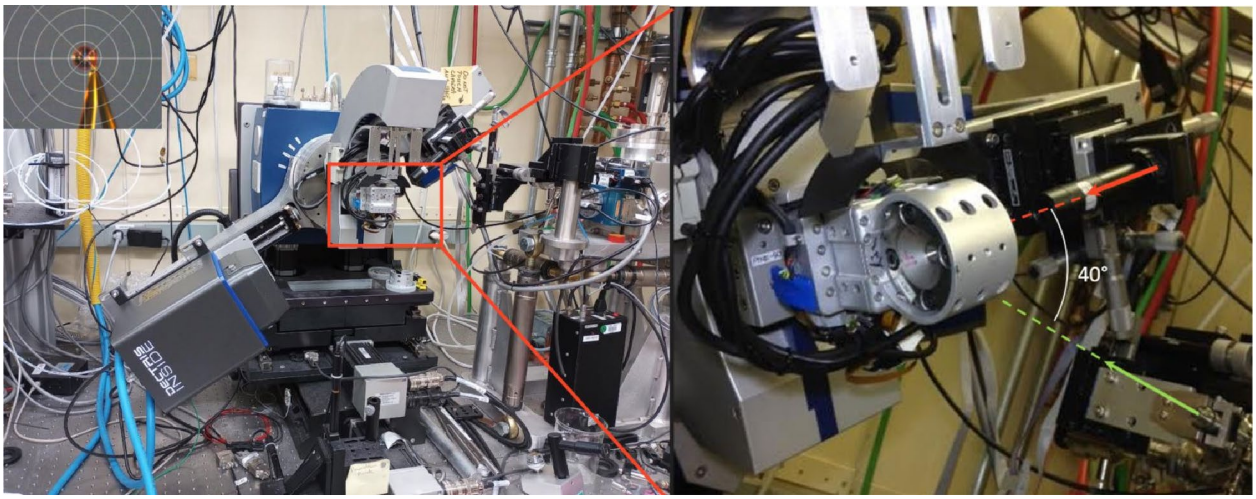

Fig. 6 Left Panel: STOE StadiVari X-ray diffractometer combined with a Dectris PILATUS3 X CdTe 300K detector mounted on 2-theta arm. The insert shows a standard crystal mounted on a MiteGen MicroMesh loop. Right Panel: A DAC, the incoming beam, and the view

laser-heated diamond anvil cell experiments in axial geometry, which remains its primary technique. Details on the LHDAC equipment and its development and characterization can be found in Caldwell et al. (2007), Kunz et al. (2018), Stan et al. (2018), and Yen et al. (2020).

A new and, to our knowledge, currently unique development that has been implemented on beamline 12.2.2 is the ability to perform double-sided laser heating on diamond anvil cells in radial geometry. This adds the possibility of performing texture and viscosity measurements in situ within the LHDAC at conditions of the Earth's interior.

12.2.2: ES2—LHDAC in radial geometry

To decipher the dynamic behavior of the deep Earth, in addition to its geochemical and mineralogical composition and geological structure, it is necessary to understand how the solid mantle maintains sufficient plastic flow to sustain convective circulation, which ultimately drives the plate movements at the surface and thus the mass exchange between the inner Earth and its surface. For this, information on the deformation and strength of rocks at the pressure (P) and temperature (T) conditions of the Earth's interior are needed. Diamond anvil cells (DACs) are ideal tools to investigate Earth materials at such conditions.

The DAC technique that allows probing strength and texture of a sample is referred to as radial X-ray diffraction (Bassett 1979; Geng et al. 2018; Kaercher et al. 2016; Kinsland and Bassett 1976; Mao et al. 1996; Merkel 2006; Merkel et al. 2013, 2004; Merkel and Yagi 2005; Miyagi et al. 2010, 2008; Miyagi and Wenk 2016; Raju et al. 2018; Speziale et al. 2019; Wenk et al. 2006; Yue et al. 2019).

While radial Diamond Anvil Cells (rDAC) are today the principal experimental technique for exploring deformation mechanisms at conditions of the Earth's lower mantle and core, they are acknowledged to have some intrinsic challenges (Wenk et al. 2006). A prominent difficulty for rDACs has been the addition of high temperature. An initial attempt at closing this gap resorted to a one-sided laser heating apparatus (Kunz et al. 2007) at the ALS in 2007. The drawback of this approach (besides the cumbersome alignment procedure) is the potential addition of an axial temperature gradient to the already inherent radial temperature gradient over the probed hot-spot. The problem of large temperature gradients has been addressed in an alternative approach, combining rDACs with resistive heating using a graphite heater that enveloped a mica-boron gasket assembly (Liermann et al. 2009; Miyagi et al. 2013). This method is, however, inherently limited to temperatures <1500 K (corresponding only to upper mantle depths of <500 km). Temperatures in excess of 3000 K, as expected in the basal portions of the lower mantle, can only be reached by means of internal laser heating.

Here, we describe an apparatus installed at ALS beamline 12.2.2 which allows the straightforward combination of a diamond anvil cell in radial geometry with double-sided laser heating.

The system is implemented on the laser heating system on ALS beamline 12.2.2 (Kunz et al. 2005, 2018; Yen et al. 2020). In contrast to the previous single-sided system (Kunz et al. 2007), where the rDAC was positioned with the principal stress axis vertical and normal to the incident X-rays, the rDAC in the double-sided system has its compression axis horizontal but perpendicular to the incident beam and thus normal to a vertical rotation axis, which is aligned onto the focused X-ray beam. The heating and pyrometry optics are inserted such that they modify the laser path of the axial system semi-automatically with minimal manual intervention.

As shown in the schematics on Fig. 7, the two sides are referred to as the 90° side (right side, viewing downstream) and 270° side (left side, viewing downstream).

The 90° side is on the right side when looking downstream. It is mounted on a vertically-positioned breadboard that carries the axial upstream and downstream laser and pyrometry equipment, including stages carrying the axial laser heating optics (Kunz et al. 2018). For this, a motorized stage equipped with a pair of adjustable elliptical mirrors (Thorlabs PFE-10-P01 within Thorlabs H45E1 on Thorlabs KM100) is mounted onto the downstream side of the breadboard such that it can be moved to intercept and redirect the laser, imaging, and pyrometry beam paths immediately before the downstream axial objective lens (Fig. 7) onto a separate 80 mm objective lens (f/2.85 apochromatic objective lens by Jenoptik Inc). The 270° equipment is situated on the left side when viewing downstream, i.e., the side which is used for manual access to the sample stage. This makes a permanent automated installation impractical, so we opted for a simple, transferable stage carrying the redirecting mirror optics and objective lens.

In order for the 270° stage to intercept the laser beam, the upstream objective lens and carbon mirror are removed (Fig. 7). The axial carbon mirrors are mounted on magnetic kinematic bases (Thorlabs KB1X1), which facilitates the transition to radial mode and allows very reproducible positioning without realignment. The base of the stage (0.5″ × 3″ × 12″ Al) is bolted onto the optical table with two 1.5″ posts (Thorlabs P14). At the bottom of the optics stack is a Newport MVN80 vertical translation stage, which allows the vertical positioning of the mirror-lens assembly onto the sample. Horizontal adjustment is achieved by a Newport 443 linear stage. A Thorlabs MB6 breadboard is mounted onto a second linear stage (Newport UMR 8.25) that is oriented in line with the objective lens such that it acts as a focusing stage. The breadboard carries two one-inch protected silver coated IR mirrors (Thorlabs PF10-03-P01), each mounted onto a kinematic mirror mount (Newport Performa-i), and an 80 mm objective lens (f/2.85 apochromatic objective lens by Jenoptik Inc), also on a kinematic mount (Thorlabs KM100R). In order to maintain operational flexibility around the sample stage while in the radial laser heating configuration, the objective lens and its mount are held by two small magnetic kinematic bases (Thorlabs KB1X1) that allow quick and reproducible removal and repositioning of the delicate objective lens. To facilitate aligning the 270° optical path orthogonal and centered, the two mounts carrying the IR mirrors are mounted on Newport M423 stages,

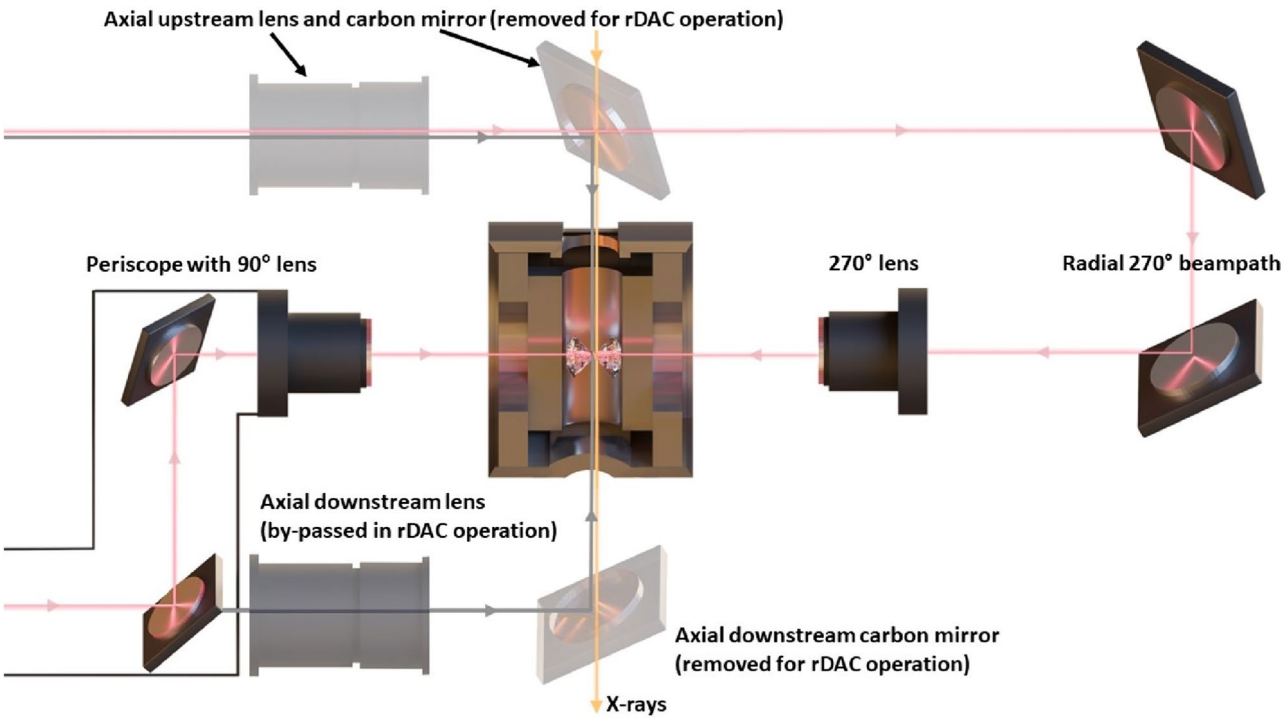

Fig. 7 Schematic of in situ laser heating system for DACs in radial diffraction configuration on ALS beamline 12.2.2. The double-sided axial laser/image/pyrometry beam-path is rotated by 90 degrees into a radial diffraction geometry by means of a motorized periscope mirror assembly (90°-side) and a manually installed mirror and lens set-up (270°-side). The X-ray beam path is depicted in yellow (top is upstream). The radial laser beam paths are given in pink. The axial laser beam paths are shown in grey with the axial optical elements grayed out for reference. The upstream axial lens and mirror and the downstream mirror are manually removed. The downstream axial lens is by-passed by the periscope assembly. The pyrometry path follows the radial laser path in reverse

allowing independent alignment of the two mirrors onto the incoming laser and focusing lens.

Setting up the system is straightforward. As mentioned above, the 90° side is fully automated and remotely controlled, thus enabling single-sided in situ laser heating within minutes. The manual installation and alignment of the 270° equipment typically takes less than an hour and can be performed independently by experienced users. The equipment not only rotates the laser path by 90 degrees relative to its default axial geometry, but also redirects the optical path for in situ pyrometry. The same pyrometric system as used in the axial geometry can therefore be employed, including quasi-instantaneous temperature mapping of the hot spot (Kunz et al. 2018). The alignment of the rig onto the intercepted IR laser and pyrometry beam path on the one hand and the sample (and thus X-rays) on the other hand is fast and easy thanks to the large number of degrees of freedom allowing independent movement of every optical component of the system. Stable heating up to several thousand K during extended periods of time (up to 30 min) without any temperature induced distortions or translations indicate that the system is mechanically stable despite its high degree of alignment flexibility.

Application of double-sided rDAC set-up to understand deformations in the lower mantle

The lower mantle consists of perovskite-structured $MgSiO_3$ (bridgmanite) and Mg-rich (Mg,Fe)O (ferropericlase) (e.g. Ringwood (1991)). To understand how the geology of the lower mantle affects tectonic processes such as earthquakes and volcanism we need to understand the deformation behavior of its main constituent minerals on a molecular scale. Plastic deformation of these rocks can lead to texture development and associated seismic anisotropy. If a detailed understanding of the link between deformation and seismic anisotropy is established, observations of seismic anisotropy can be used to understand the dynamics of the deep Earth. Two separate experiments on beamline 12.2.2 investigated the deformation behavior of bridgmanite and magnesiowüstite (Fe-rich ferropericlase) using the new double-sided laser heating rDAC capability:

Deformation of bridgmanite at high pressure and high temperature

Finely-ground $MgSiO_3$ enstatite starting material was mixed with Pt into a 30 µm sample chamber within a cBN/Kapton gasket on 300µm/100µm beveled diamond anvil culets. The sample was compressed to 45 GPa and then converted to bridgmanite by double sided laser heating. This bridgmanite sample was further compressed while laser heating to obtain its deformation texture in situ at simultaneous high pressures and temperatures. The process was monitored in situ using 25 keV X-rays and a Mar345 image plate detector. Detector and beamline geometry as well as diffraction widths were calibrated using a NIST-SRM674b CeO_2 standard. Data were reduced and analyzed using a combination of fit2d (Hammersley 2016), MAUD (Lutterotti et al. 1999) and BEARTEX (Wenk et al. 1998). Details on laser heating pyrometry can be found in Kunz et al. (2018), Yen et al. (2020) and Rainey and Kavner (2014).

We find that after conversion from enstatite to bridgmanite at 48 GPa, any compressional texture of enstatite has been erased leaving the newly formed bridgmanite grains with random orientation (Fig. 8). However, during high temperature deformation at ~1600 K and 52 GPa two main maxima form, one at (001) and a second at (100). Further compression to 80 GPa at 1600 K strengthens both maxima. Upon temperature quenching to 300 K the maxima at 100 and 010 decrease in intensity but the (001) maximum remains. A comparison of our results to previous results in the literature (Couper et al. 2020; Miyagi and Wenk 2016) suggests that a change in slip system occurs from (001) at room temperature to (100) at high temperature. The mixed (001), (100) maxima found in our in situ laser heating experiments point to an intrinsic disadvantage of in situ laser heated rDAC experiments: based on the geometry in which the X-rays probe the sample disk with a hot spot in the center along its radial direction, the beam necessarily probes both cold and hot regions of the experiment. Conversely, this serves to

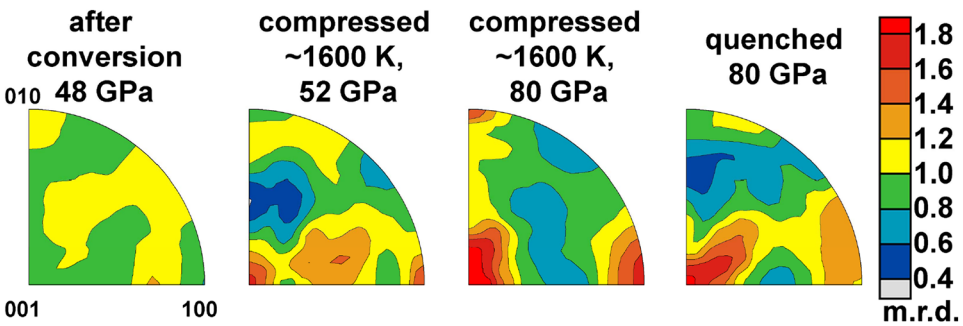

Fig. 8 Inverse Pole Figure (IPF) of the compression direction for in situ high temperature deformation of bridgmanite. M.r.d is multiples of random distribution with 1 m.r.d being random distribution

show that within a given sample with temperature gradients, different slip systems can co-exist and be characterized using this technique.

Deformation and phase transitions in $Fe_{0.92}O$ at high pressure and high temperature

Wüstite (FeO) is the iron end-member of the (Mg,Fe)O solid solution that constitutes the second major phase in the lower mantle after bridgmanite. It forms a continuous solid solution with periclase (MgO). Iron in the lower mantle [often considered to be present between 6 and 7.5 wt% FeO (Poirier 2000)] is believed to preferentially partition into Mg-wüstite (Sakai et al. 2009). Low Mg wüstite may be an important component of ultra-low velocity zones at the base of the mantle (Whittaker et al. 2016; Wicks et al. 2010). Periclase (MgO) and wüstite (FeO) both crystallize in the NaCl (B1) structure at ambient conditions. However, FeO exhibits a more complex P–T phase diagram than MgO (Duffy et al. 1995; Fei 1996; Fischer et al. 2011). While MgO stays in the B1 NaCl structure within the P–T range of interest in the Earth's mantle, a series of phase transitions have been reported over the years for $Fe_{1-x}O$ (Fischer et al. (2011) and references therein); most notably a rhombohedral R-3 structure (distortion along the cube diagonal) at above ~17 GPa, as well as a B1–B8 transition at high pressure and high temperature. At 10 K and room pressure $Fe_{0.99}O$ was found to have a monoclinic C2/m structure using high resolution neutron diffraction (Fjellvåg et al. 2002). A monoclinic $P2_1/m$ phase has also been reported at 75 GPa (Kantor et al. 2008).

Here we report on reproducible and unambiguous transitions from the high temperature B1 phase to a monoclinic phase in a double-sided laser heated rDAC.

$Fe_{0.92}O$ was loaded into a radial diamond BX90 anvil cell (rDAC). Diamond culet diameter was 200 µm. The sample chamber was a 60 µm diameter hole which was laser drilled from a 40 µm thick and 360 µm in diameter cBN gasket and confined by a Kapton jacket (Miyagi et al. 2013). The monochromatic X-ray beam from ALS beamline 12.2.2 ($\lambda = 0.4959$ Å) was focused to a size of ~10 µm FWHM. Wavelength, detector distance, and detector tilt were calibrated in Dioptas (Prescher and Prakapenka 2015) using a NIST-SRM674b CeO_2 standard. Diffraction images of $Fe_{0.92}O$ were collected for 60 s on a Mar345 image plate located ~335 mm from the sample. Data were analyzed using Dioptas, MAUD (Lutterotti et al. 1999) and BEARTEX (Wenk et al. 1998). Details on laser heating pyrometry can be found in Yen et al. (2020) and Rainey and Kavner (2014).

A monoclinic phase of $Fe_{0.92}O$ was formed at pressures >23 GPa under deviatoric stress and observed using in situ X-ray diffraction in a radial diamond anvil cell. Based on visual analysis of peak splitting (Fig. 9), an initial phase transition from the rhombohedral phase is suspected to occur between 23 and 27 GPa. Following laser heating, monoclinic peaks are clearly identifiable as distinct from a highly anisotropic rhombohedral structure. This structure can be fit with the C2/m structure as identified by Fjellvåg et al. (2002). The monoclinic structure is consistently reproducible from the high-temperature cubic phase at these pressures, and is stable during compression at least up to 36 GPa. The stability of the monoclinic unit cell is likely dependent on both the degree of non-hydrostaticity within the sample chamber and the high defect density of $Fe_{0.92}O$ as compared to $Fe_{1-x}O$ samples that are closer to stoichiometric. Temperature may also have acted as a catalyst for the phase transformation, and/or the heating sufficiently relaxed elastic strain in the quenched crystal lattice such that highly strained monoclinic peaks present prior to heating were then identifiable.

Using simultaneous X-ray diffraction in radial geometry and double-sided laser heating, texture relationships between the high-temperature B1 structure and the ambient temperature monoclinic structure could be established. As the B1

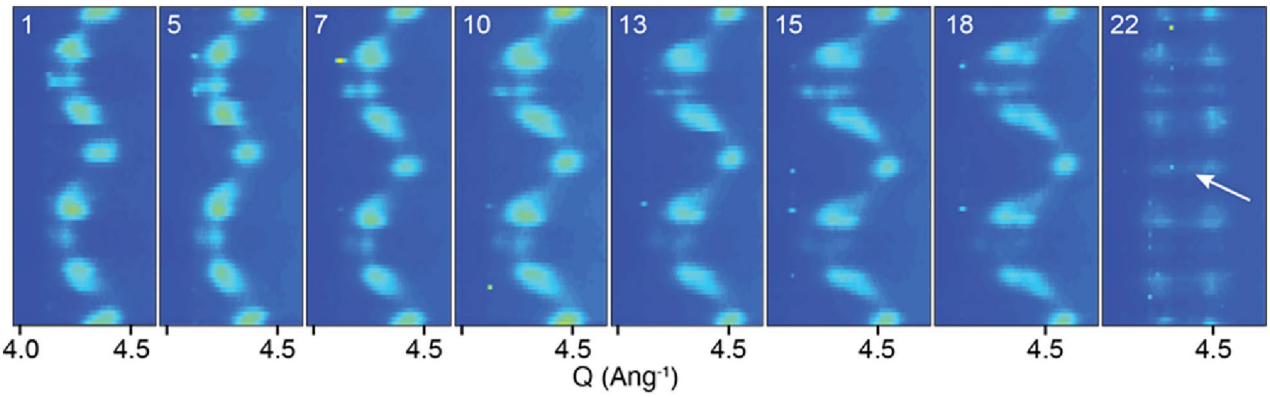

Fig. 9 Progression of splitting of the cubic 220 diffraction line during compression at room temperature (image 1–18) and after a single, consecutive stage of laser heating (image 22). Each panel shows an unrolled diffraction image composed of 72 5° azimuthal sector integrations. A faint diffraction line in image 22 is indicated by a white arrow

structure is unquenchable, this could not have been determined by conventional laser heating of a radial diamond anvil cell in axial geometry.

Texture developments are summarized in Fig. 10 using inverse pole figures (IPF). Inverse pole figures are reported before and after major phase transitions and following periods of compression (Fig. 10). At the beginning of the experiment (15 GPa), maxima in the cubic $Fe_{0.92}O$ IPF are concentrated at 001 (~3–4.0 m.r.d.) and 011 (~2–3 m.r.d.; Fig. 10a). Preferred orientation in the cubic phase becomes more pronounced at 001 (~5–6 m.r.d.) in the IPF during the phase transformation (Fig. 10b). Primary maxima development in the trigonal IPF is at 211 (>7 m.r.d.; Fig. 10b). After a complete transformation to the trigonal phase at 19 GPa and 300K, IPF intensities are roughly equal at 211 and near 2–21 (~3.0–4.5 m.r.d.; Fig. 10c). Further compression to 23 GPa (Fig. 10d) results in textures similar to those of Kaercher et al. (2012) at 19 GPa. From both graphical and a Rietveld Rwp analysis, we interpret that a phase change occurs above 23 GPa (Fig. 9).

The monoclinic IPF at conditions of ~27 GPa and 300 K shows maxima at 001 (~5–6 m.r.d.), near both 101 and − 101 (~4–5 m.r.d.), and at 211 (~3–4 m.r.d.; Fig. 10e). Further compression of the monoclinic phase does not result in significant changes in texture (Fig. 10e, f). During the first stage of heating (39 GPa, 1500 K), only one laser coupled with the sample, and both cubic and monoclinic phases are present. We anticipate that a strong temperature gradient was present due to only one laser having coupled, and suggest that the monoclinic phase is present only in cooler regions of the sample chamber. The cubic IPF shows both 001 and 011 fibers perpendicular to compression after transformation (~3–4 m.r.d, Fig. 10g). A maximum at 001 in the monoclinic IPF present prior to heating weakens during heating (2–3 m.r.d.), and the maxima near 101 and − 101 (>7 m.r.d.) become elongated between 001 and 100.

Post-heating, the maximum in the monoclinic IPF at 001 is weaker (~3–4 m.r.d.; Fig. 10h) as compared to pre-heating (Fig. 10f). The intensity in the IPF is concentrated near − 101 and 101 (~6–7 m.r.d.; Fig. 10h). Maxima in the monoclinic IPF at 011 and 211 both have moderate intensities (~3.0–4.0 m.r.d.).

Only the cubic phase is visible in the second round of heating at ~1400 K, where both lasers coupled to the sample. Texture in cubic $Fe_{0.92}O$ (Fig. 10i) is relatively unchanged from that of 39 GPa, 1500 K (Fig. 10g). No monoclinic phase is present. The monoclinic phase returns when the sample is allowed to cool to room temperature (Fig. 10j). The maxima at 001 and near − 101 and 101 in the monoclinic IPF have weakened compared to the previous

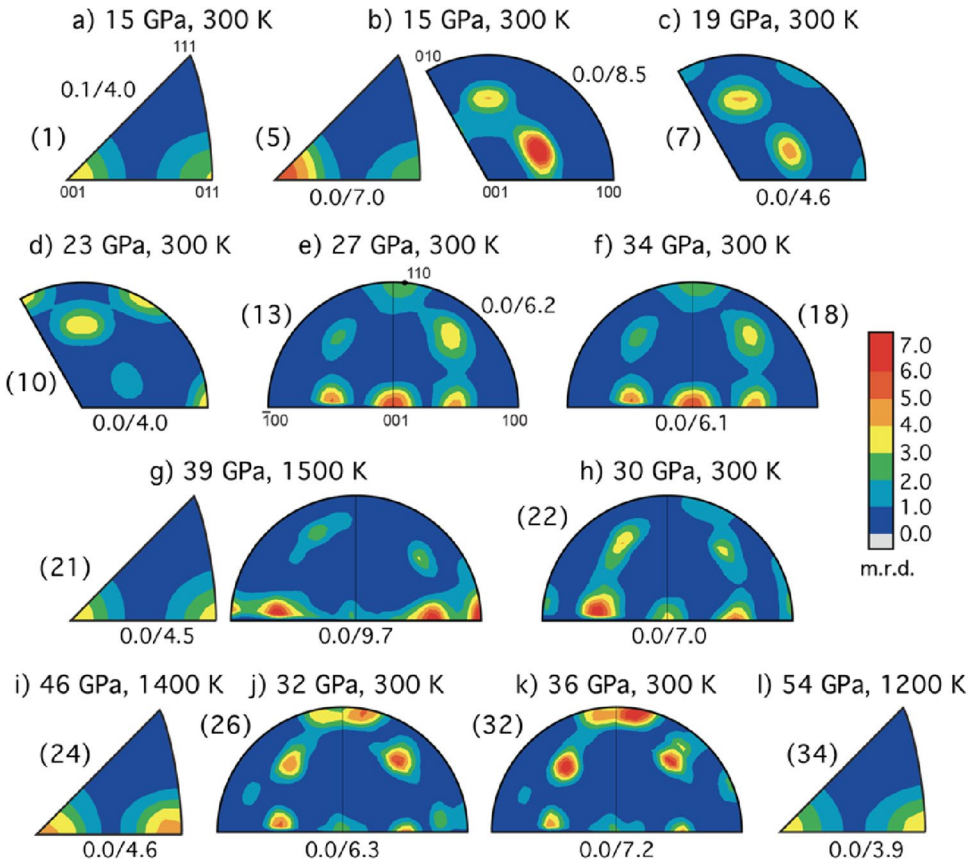

Fig. 10 Inverse pole figures (IPFs) showing texture development in the direction of compression for $Fe_{0.92}O$ polymorphs over the course of this study. Pressure and temperature at the time of image collection are shown above the IPF. Corresponding image numbers are shown in parenthesis. For monoclinic phases, pressures were determined from the best fit of a trigonal unit cell (Jacobsen et al. 2005). A backslash (/) separates minimum and maximum multiples of random distribution (m.r.d.) values for each IPF

monoclinic phase (~2–3 m.r.d.), and maxima have strengthened both at 211 (4–5 m.r.d.) and near 011 (~5–6 m.r.d.). An additional maximum is also seen near to the top of the monoclinic IPF (~5–6 m.r.d.; Fig. 10j). As the monoclinic phase is compressed, maxima at 211 and 011 and at the top of the IPF (Fig. 10k) continue to develop. When transformed into the cubic phase at 1200 K, the cubic IPF has two maxima of moderate intensities at 001 and 011 (~3–4 m.r.d.; Fig. 10l).

Hence, these results illustrate both the capabilities of the laser-heated radial diffraction system at beamline 12.2.2, and the notable phase and deformational complexity that can be present even within a comparatively chemically simple system at mid-mantle pressures.

X-ray Laue microdiffraction: beamline 12.3.2

Beamline 12.3.2 was commissioned in 2008, after moving the successful bending magnet Laue X-ray microdiffraction program on beamline 7.3.3 (Tamura et al. 2003) to a 4.37 T superconducting magnet source to increase the flux and energy range (Kunz et al. 2009b). While the original scientific focus of the beamline was the measurement of strains in electronic materials using Laue X-ray microdiffraction (Valek et al. 2002), its program has expanded to include a variety of fields ranging from geosciences to solid state physics and a variety of techniques, including powder microdiffraction and microfluorescence.

The first optic on the path of the synchrotron beam is a horizontally deflecting toroidal mirror, which refocuses the source at the entrance of the experimental hutch, where a pair of roll slits provides a size-adjustable secondary source. The optic chamber inside the hutch contains a pair of JTEC water-cooled Kirkpatrick-Baez mirrors with fixed elliptical shapes that produce a 1 µm X-ray beam on the sample. A 4-bounce Si(111) double channel-cut monochromator can be inserted into the beam to easily switch between polychromatic and monochromatic beams while illuminating the same spot on the sample. The available energy range for the beamline is about 6–24 keV, with a peak intensity around 12 keV. The flexible sample and detector stages allow for both transmission and reflection geometries. 2D diffraction patterns are collected with a DECTRIS Pilatus 1 M, while X-ray microfluorescence signals are collected using a Vortex EM solid-state detector. Additional sample environment chambers are employed to heat samples up to about 1000 K or cool them to about 180 K. A new cooling stage will be made available in the near future, that will be able to cool samples down to liquid N_2 temperatures.

To date, only a few experiments have been conducted under non-ambient conditions at 12.3.2, largely because it was not originally intended for non-ambient condition research. Some of its unique capabilities show promise, however, particularly in the study of plastic deformation in nanocrystalline materials, a topic that is not well understood. One such study used a diamond anvil cell to perform high-pressure Laue X-ray microdiffraction to investigate the size dependence of nickel nanocrystal grain rotation (from 500 nm down to 3 nm) (Zhou et al. 2017), as grain rotation resulting from grain boundary dislocations is one manifestation of plastic deformation in materials.

6–8 µm tungsten carbide (WC) particles were embedded into a nickel medium of variable particle sizes to act as fiducial markers for the rotation of the nickel nanocrystals. Laue patterns were collected on the WC particles to measure their crystal orientations, and thus their rotations relative to their starting position, at pressures up to 10 GPa. Models such as the Read–Shockley model predict that grain rotation increases with decreasing nanocrystal size. However, the experiment demonstrated that the 70 nm nickel medium induced more rotation than in any other nickel medium, whether larger or smaller in particle size. Subsequent measurements of texture deformation performed at beamline 12.2.2 on the same samples indicated that dislocations in the interior of the grains remain active in grains down to 20 nm. This suite of complementary measurements at two ALS beamlines thus demonstrated that nanocrystal grain rotations are governed by dislocations both in grain interiors and along grain boundaries under external stresses, and the two opposing trends are what caused the observed maximal grain rotation of nanocrystals of a specific size. This study provides a better understanding of plastic deformation in nanocrystalline materials and provides guidance for material properties, functionalities, design, and processing.

In Earth science, Laue X-ray microdiffraction (Laue µXRD) has been widely used to examine and map lattice distortion in quartz at the micron scale (Chen et al. 2015; Kunz et al. 2009a). The shape and orientation of the elastic strain tensor can be derived from lattice distortions and explained in terms of residual stress. It was shown that mechanically-induced Dauphine twinning, rhombohedral deformation lamellae, and residual stresses in the Vredefort quartzite are features of shock deformation from the meteorite impact site at Vredefort, South Africa (Chen et al. 2011). For another study, the microstructures of core samples from the San Andreas Fault Observatory at Depth (SAFOD) were shown to comprise complex compositions of quartz, feldspar, clays, and amorphous material, indicating that the primary deformation processes were intense shearing and dissolution–precipitation. The differential stresses are inferred to range from 33 to 132 MPa, with mean values falling between 68 and 168 MPa. The inferred friction coefficient was found to be quite low, assuming hydrostatic pore pressure. The measurements performed support the hypothesis of a weak San Andreas Fault (Rybacki et al. 2011).

Laue μXRD was also used to investigate vein quartz from Bastogne, Belgium, the original boudinage locality. The measurements showed a residual elastic strain that involves shortening perpendicular to the vein wall (Fig. 11) supporting the hypothesis that the Bastogne boudins formed by layer-parallel shortening rather than layer-parallel extension, as had been previously assumed (Chen et al. 2016).

Additional experiments reveal that metasedimentary quartzites from the Bergell Alps generally shorten perpendicular to the schistosity plane, but with significant asymmetry in relation to foliation and lineation. Laue μXRD is thus a promising technique to detect stress fields during tectonic deformation (Wenk et al. 2020).

Another beamline capability that may be of broader interest is the structure refinement and solution of crystals by Laue μXRD that are either too small or encased in a heterogeneous matrix so that they cannot be studied by conventional crystallographic methods (Dejoie et al. 2013). These methods have been successfully employed in the discovery and naming of eight new minerals since 2019 [including new Pt-group minerals], (Barkov et al. 2019a, b, 2021). In principle, this technique can be applied to crystals synthesized inside a diamond anvil cell or trapped as inclusions in high-pressure charges.

Off-line capabilities

Many of the experiments performed at the ALS require extensive, delicate sample preparation, particularly high-pressure diamond anvil cell experiments. Users typically prepare their samples at their home institutions, however sample reloading during beamtime is often required. In addition, DAC experiments often require the addition of a gaseous pressure medium into the sample chamber (referred to as gas loading), however many users lack the complex and expensive equipment necessary to gas load a DAC. To address these needs, the ALS has allocated laboratory space near the beamline where 12.2.2 users may prepare and load DACs. The laboratory is well-equipped for DAC sample preparation, hosting three Leica M205C stereomicroscopes as well as an Oxford Lasers Alpha 532 laser milling system. The laser mill primarily serves to machine gaskets for DAC experiments and is capable of drilling sample chambers with <5 μm accuracy. The laser mill control software (Cimita v4.3.3) is user-friendly and the instrument is available to beamline users after minimal training. To gas load samples, the laboratory houses a COMPRES/GSECARS gas loading apparatus (Rivers et al.

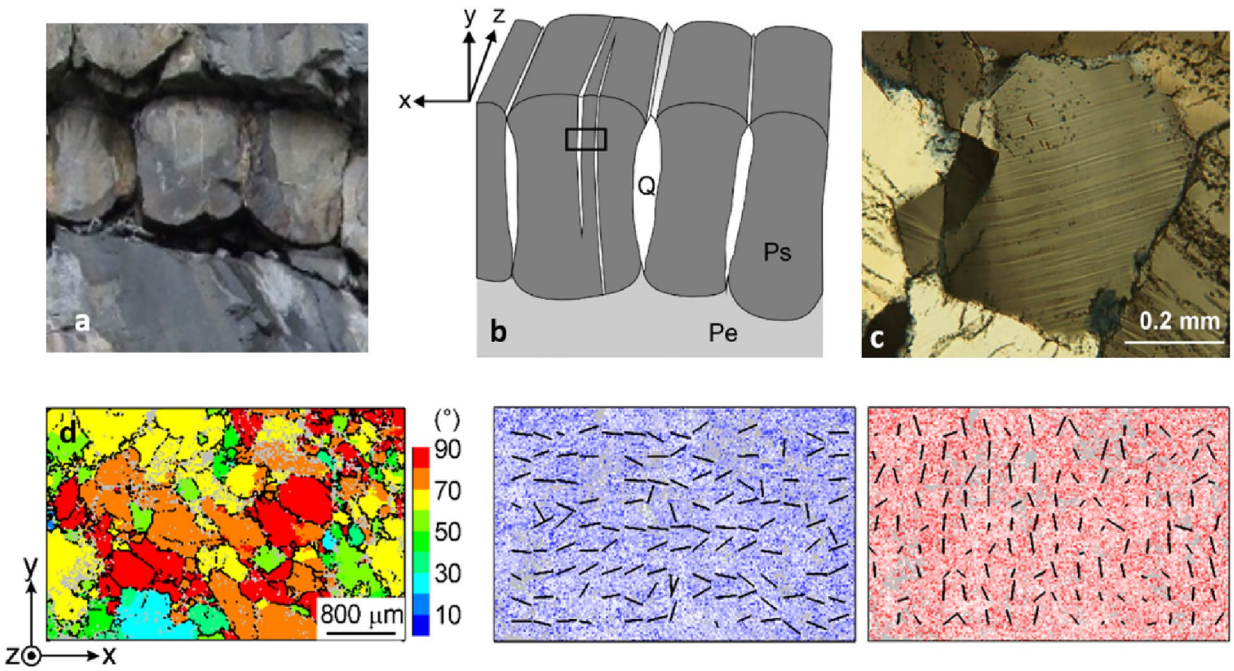

Fig. 11 **a** View of psammite(Ps)-pelite(Pe) multilayer sequence in the Mardasson quarry near Bastogne (50°00′55.01″N, 5°44′27.63″E) with the typical "boudin" structures, separated by quartz veins, in the stiffer psammite layers. **b** Schematic line drawing (not to scale) of the Bastogne "boudin" structure (Q: vein quartz, Ps psammite and Pe pelite), indicating the sample location with two quartz veinlets; sample coordinates are indicated (xyz). **c** Detail of one of the scanned quartz grains with deformation lamellae and fluid inclusions. **d** results from a large scan on a quartzite lamella with grain orientation (Euler orientation angle (ϕ) and boundaries (left), and magnitudes of the compressional (blue, middle) and extensional principal strain axes (red, right) of the strain ellipsoid and their directions projected on the x–y plane (black lines)). Figure adapted from (Chen et al. 2016)

2008). Though the gas loader is not available for users to operate independently, users may request that beamline staff load their DACs with He, Ne, or Ar in advance of their shift, with other gasses such as CO_2 potentially available on request. While the sample preparation lab is maintained and operated by 12.2.2 staff, it is available upon request and coordination to users of any ALS beamline.

Acknowledgements The Advanced Light Source is a DOE Office of Science User Facility under contract no. DE-AC02-05CH11231. Part of this work (8.3.2 section) was also supported by the U.S. Department of Energy, Office of Science, Office of Basic Energy Sciences, Chemical Sciences, Geosciences, and Biosciences Division, through its Geoscience program at LBNL under the same contract number. L.M. acknowledges support from the NSF (EAR-2054993) and US Department of Energy National Nuclear Security Administration through the Chicago-DOE Alliance Center (DE- NA0003975). Q.W. acknowledges support from NSF EAR-2017294. A portion of both the ongoing staffing and infrastructure at beamline 12.2.2 has been funded since 2004 under the aegis of COMPRES, the National Science Foundation-funded Consortium for Materials Properties Research in the Earth Sciences under NSF Cooperative Agreement EAR 1606856. An explicit goal of this enterprise was enabling Earth sciences users to access state-of-the-art beamlines at Department of Energy facilities. From a logistical standpoint, at the Advanced Light Source, this synergistic relationship between two administratively distinct agencies on behalf of the high-pressure Earth sciences community is accomplished via the ALS Approved Program mechanism. In most instances, this vehicle is oriented towards providing a guaranteed amount of beamtime each cycle for a single particularly active group on a timely and distinct research direction. In the case of COMPRES, the guarantee has been for 35% of the beamtime at beamline 12.2.2, but a supplementary arrangement has been orchestrated in which beamtime for COMPRES users is allocated via the ALS' General User Program, rather than by the Approved Program Principal Investigator, as is typical. The COMPRES initiative was replaced in late 2023 by a new, NSF-funded community-driven organization—SEES: Synchrotron Earth and Environmental Science. SEES is supported by the National Science Foundation Division of Earth Sciences (EAR) via EAR-2223273. The logistics of the new organization interfacing with the ALS are similar to those developed during COMPRES, although the scientific footprint of the new organization is broader, and hence its footprint at the ALS will extend beyond beamline 12.2.2.

Author contributions M. Kunz wrote 12.2.2 ES-2 section and coordinated manuscript writing; K. Armstrong contributed to 12.2.2 section and off-line capabilities section; H. Barnard contributed to 8.3.2 section; H.A. Bechtel wrote IR section; B. Kalkan wrote 12.2.2 ES-1 section; H. Lisabeth contributed to 8.3.2 section; A.A. MacDowell contributed to 8.3.2 and 12.2.2 sections; D.Y. Parkinson contributed to 8.3.2 section; N. Tamura wrote 12.3.2 section; Q. Williams contributed to 12.2.2 section and introduction; L. Miyagi contributed with experiments and manuscript writing (12.2.2 section); and S. Couper contributed with experiments (12.2.2 section)

Data availability Raw data are stored on beamlime servers of the various beamlines discussed and can be obtained upon request.

Declarations

Conflict of interest The authors have no competing interests to declare that are relevant to the content of this article.

Open Access This article is licensed under a Creative Commons Attribution 4.0 International License, which permits use, sharing, adaptation, distribution and reproduction in any medium or format, as long as you give appropriate credit to the original author(s) and the source, provide a link to the Creative Commons licence, and indicate if changes were made. The images or other third party material in this article are included in the article's Creative Commons licence, unless indicated otherwise in a credit line to the material. If material is not included in the article's Creative Commons licence and your intended use is not permitted by statutory regulation or exceeds the permitted use, you will need to obtain permission directly from the copyright holder. To view a copy of this licence, visit http://creativecommons.org/licenses/by/4.0/.

References

Anzellini S, Dewaele A, Mezouar M, Loubeyre P, Morard G (2013) Melting of iron at Earth's inner core boundary based on fast X-ray diffraction. Science 340:464–466

Barkov AY, Tamura N, Shvedov GI, Stan CV, Ma C, Winkler B, Martin RF (2019a) Platiniferous tetra-auricupride: A case study from the Bolshoy Khailyk placer deposit, Western Sayans. Russia. Miner 9(3):160

Barkov AY, Bindi L, Tamura N, Shvedov GI, Winkler B, Stan CV, Morgenroth W, Martin RF, Zaccarini F, Stanley CJ (2019b) Ognitite, NiBiTe, a new mineral species, and Co-rich maucherite from the Ognit ultramafic complex, Eastern Sayans, Russia. Mineral Mag 83:695–703

Barkov AY, Bindi L, Tamura N, Martin RF, Ma C, Winkler B, Shvedov GI, Morgenroth W (2021) Fleetite, Cu2RhIrSb2, a new species of platinum-group mineral from the Miass placer zone, Southern Urals, Russia. Can Miner 59:423–430

Bassett WA (1979) The diamond cell and the nature of the Earth's mantle. Annu Rev Earth Planet Sci 7:357–384

Bechtel HA, Muller EA, Olmon RL, Martin MC, Raschke MB (2014) Ultrabroadband infrared nanospectroscopic imaging. Proc Natl Acad Sci 111:7191–7196. https://doi.org/10.1073/pnas.1400502111

Bechtel HA, Johnson SC, Khatib O, Muller EA, Raschke MB (2020) Synchrotron infrared nano-spectroscopy and-imaging. Surf Sci Rep 75:100493. https://doi.org/10.1016/j.surfrep.2020.100493

Bommannavar A, Chow P, Ferry R, Hrubiak R, Humble F, Kenney-Benson C, Lv M, Meng Y, Park C, Popov D (2022) Overview of HPCAT and capabilities for studying minerals and various other materials at high-pressure conditions. Phys Chem Miner 49:36. https://doi.org/10.1007/s00269-022-01209-2

Bouskill NJ, Wood TE, Baran R, Hao Z, Ye Z, Bowen BP, Lim HC, Nico PS, Holman H-Y, Gilbert B (2016) Belowground response to drought in a tropical forest soil. II. Change in microbial function impacts carbon composition. Front Microbiol 7:323. https://doi.org/10.3389/fmicb.2016.00323

Calas G, Bassett W, Petiau J, Steinberg M, Tchoubar D, Zarka A (1984) Some mineralogical applications of synchrotron radiation. Phys Chem Miner 11:17–36. https://doi.org/10.1007/BF00309373

Caldwell WA, Kunz M, Celestre RS, Domning E, Walter M, Walker D, Glossinger J, MacDowell AA, Padmore H, Jeanloz R (2007) Laser-heated diamond anvil cell at the advanced light source beamline 12.2.2. Nucl Instrum Methods Phys Res Sect A 582:221–225. https://doi.org/10.1016/j.nima.2007.08.113

Chen K, Kunz M, Tamura N, Wenk H-R (2011) Evidence for high stress in quartz from the impact site of Vredefort, South Africa. Eur J Mineral 23:169–178. https://doi.org/10.1127/0935-1221/2011/0023-2082

Chen K, Kunz M, Tamura N, Wenk H-R (2015) Residual stress preserved in quartz from the San Andreas Fault Observatory at Depth. Geology 43:219–222. https://doi.org/10.1130/G36443.1

Chen K, Kunz M, Li Y, Zepeda-Alarcon E, Sintubin M, Wenk HR (2016) Compressional residual stress in Bastogne boudins revealed by synchrotron X-ray microdiffraction. Geophys Res Lett 43:6178–6185. https://doi.org/10.1002/2016GL069236

Chen H, Leinenweber K, Prakapenka V, Prescher C, Meng Y, Bechtel H, Kunz M, Shim S-H (2020) Possible H_2O storage in the crystal structure of $CaSiO_3$ perovskite. Phys Earth Planet Inter 299:106412. https://doi.org/10.1016/j.pepi.2019.106412

Cnudde V, Boone MN (2013) High-resolution X-ray computed tomography in geosciences: a review of the current technology and applications. Earth Sci Rev 123:1–17

Coppens P (1970) The evaluation of absorption and extinction in single crystal structure analysis. In: Ahmed FR, Hall SR, Huber CP (eds) Crystallographic computing: proceedings of an international summer school organized by the commission on crystallographic computing of the international union of crystallography and held in Ottawa, 4–11 August 1969, Munksgaard, Copenhagen, pp 4–11

Couper S, Speziale S, Marquardt H, Liermann H-P, Miyagi L (2020) Does heterogeneous strain act as a control on seismic anisotropy in Earth's lower mantle? Front Earth Sci 8:540449

Dejoie C, McCusker LB, Baerlocher C, Kunz M, Tamura N (2013) Can Laue microdiffraction be used to solve and refine complex inorganic structures? J Appl Crystallogr 46:1805–1816. https://doi.org/10.1107/S0021889813026307

Deng H, Molins S, Steefel C, DePaolo D, Voltolini M, Yang L, Ajo-Franklin J (2016) A 2.5 D reactive transport model for fracture alteration simulation. Environ Sci Technol 50:7564–7571. https://doi.org/10.1021/acs.est.6b02184

Deng H, Voltolini M, Molins S, Steefel C, DePaolo D, Ajo-Franklin J, Yang L (2017) Alteration and erosion of rock matrix bordering a carbonate-rich shale fracture. Environ Sci Technol 51:8861–8868. https://doi.org/10.1021/acs.est.7b02063

Duffy TS, Hemley RJ, Mao H-k (1995) Equation of state and shear strength at multimegabar pressures: magnesium oxide to 227 GPa. Phys Rev Lett 74:1371

Dumas P, Martin MC, Carr GL (2020) IR spectroscopy and spectromicroscopy with synchrotron radiation. In: Jaeschke EJ, Khan S, Schneider JR, Hastings JB (eds) Synchrotron light sources and free-electron lasers: accelerator physics, instrumentation and science applications. Springer International Publishing, Cham, pp 2059–2113

Fei Y (1996) Crystal chemistry of FeO at high pressure and temperature. Miner Spectrosc A Trib Roger G Burns 5:243–254

Fenter PA, Rivers ML, Sturchio N, Sutton SR (2018) Applications of synchrotron radiation in low-temperature geochemistry and environmental science. Walter de Gruyter GmbH & Co KG, Belin

Fischer RA, Campbell AJ, Shofner GA, Lord OT, Dera P, Prakapenka VB (2011) Equation of state and phase diagram of FeO. Earth Planet Sci Lett 304:496–502

Fjellvåg H, Hauback BC, Vogt T, Stølen S (2002) Monoclinic nearly stoichiometric wüstite at low temperatures. Am Miner 87:347–349. https://doi.org/10.2138/am-2002-2-318

Garing C, de Chalendar JA, Voltolini M, Ajo-Franklin JB, Benson SM (2017a) Pore-scale capillary pressure analysis using multi-scale X-ray micromotography. Adv Water Resour 104:223–241. https://doi.org/10.1016/j.advwatres.2017.04.006

Garing C, Voltolini M, Ajo-Franklin JB, Benson SM (2017b) Pore-scale evolution of trapped CO_2 at early stages following imbibition using micro-CT imaging. Energy Procedia 114:4872–4878. https://doi.org/10.1016/j.egypro.2017.03.1628

Geng G, Vasin RN, Li J, Qomi MJA, Yan J, Wenk H-R, Monteiro PJ (2018) Preferred orientation of calcium aluminosilicate hydrate induced by confined compression. Cem Concr Res 113:186–196. https://doi.org/10.1016/j.cemconres.2018.09.002

Hammersley A (2016) FIT2D: a multi-purpose data reduction, analysis and visualization program. J Appl Crystallogr 49:646–652

Hao Z, Bechtel HA, Kneafsey T, Gilbert B, Nico PS (2018) Cross-scale molecular analysis of chemical heterogeneity in shale rocks. Sci Rep 8:2552. https://doi.org/10.1038/s41598-018-20365-6

Häusermann D (1992) Current progress and future developments in sychrotron radiation instrumentation for high-pressure research including the esrf programme. High Press Res 8:723–737. https://doi.org/10.1080/08957959208206327

Hazen TC, Dubinsky EA, DeSantis TZ, Andersen GL, Piceno YM, Singh N, Jansson JK, Probst A, Borglin SE, Fortney JL (2010) Deep-sea oil plume enriches indigenous oil-degrading bacteria. Science 330:204–208. https://doi.org/10.1126/science.1195979

Hemley R, Goncharov A, Lu R, Struzhkin V, Li M, Mao H (1998) High-pressure synchrotron infrared spectroscopy at the National Synchrotron Light Source. Il Nuovo Cimento D 20:539–551. https://doi.org/10.1007/BF03185547

Holman H-YN, Bechtel HA, Hao Z, Martin MC (2010) Synchrotron IR spectromicroscopy: chemistry of living cells. ACS Publications, Washington. https://doi.org/10.1021/ac100991d

Ishii HA, Bradley JP, Bechtel HA, Brownlee DE, Bustillo KC, Ciston J, Cuzzi JN, Floss C, Joswiak DJ (2018) Multiple generations of grain aggregation in different environments preceded solar system body formation. Proc Natl Acad Sci 115:6608–6613. https://doi.org/10.1073/pnas.1720167115

Jacobsen SD, Lin J-F, Angel RJ, Shen G, Prakapenka VB, Dera P, Mao H-K, Hemley RJ (2005) Single-crystal synchrotron X-ray diffraction study of wüstite and magnesiowüstite at lower-mantle pressures. J Synchrotron Radiat 12:577–583

Kaercher P, Speziale S, Miyagi L, Kanitpanyacharoen W, Wenk H-R (2012) Crystallographic preferred orientation in wüstite (FeO) through the cubic-to-rhombohedral phase transition. Phys Chem Miner 39:613–626

Kaercher P, Miyagi L, Kanitpanyacharoen W, Zepeda-Alarcon E, Wang Y, Parkinson D, Lebensohn R, De Carlo F, Wenk H (2016) Two-phase deformation of lower mantle mineral analogs. Earth Planet Sci Lett 456:134–145. https://doi.org/10.1016/j.epsl.2016.09.030

Kantor I, Kurnosov A, McCammon C, Dubrovinsky L (2008) Monoclinic FeO at high pressures. Z Krist Cryst Mater 223:461–464

Keiluweit M, Nico P, Harmon ME, Mao J, Pett-Ridge J, Kleber M (2015) Long-term litter decomposition controlled by manganese redox cycling. Proc Natl Acad Sci 112:E5253–E5260. https://doi.org/10.1073/pnas.1508945112

Kinsland GL, Bassett WA (1976) Modification of the diamond cell for measuring strain and the strength of materials at pressures up to 300 kilobar. Rev Sci Instrum 47:130–133. https://doi.org/10.1063/1.1134460

Koziskova J, Hahn F, Richter J, Kozisek J (2016) Comparison of different absorption corrections on the model structure of tetrakis ([mu] 2-acetato)-diaqua-di-copper (II). Acta Chim Slovaca 9:136. https://doi.org/10.1515/acs-2016-0023

Kunz M, MacDowell AA, Caldwell WA, Cambie D, Celestre RS, Domning EE, Duarte RM, Gleason AE, Glossinger JM, Kelez N (2005) A beamline for high-pressure studies at the advanced light source with a superconducting bending magnet as the source. J Synchrotron Radiat 12:650–658. https://doi.org/10.1107/S0909049505020959

Kunz M, Caldwell WA, Miyagi L, Wenk H-R (2007) In situ laser heating and radial synchrotron X-ray diffraction in a diamond anvil cell. Rev Sci Instrum 78:063907. https://doi.org/10.1063/1.2749443

Kunz M, Chen K, Tamura N, Wenk H-R (2009a) Evidence for residual elastic strain in deformed natural quartz. Am Miner 94:1059–1062

Kunz M, Tamura N, Chen K, MacDowell AA, Celestre RS, Church MM, Fakra S, Domning EE, Glossinger JM, Kirschman JL (2009b) A dedicated superbend X-ray microdiffraction beamline for materials, geo-, and environmental sciences at the advanced light source. Rev Sci Instrum 80:035108. https://doi.org/10.1063/1.3096295

Kunz M, Yan J, Cornell E, Domning EE, Yen CE, Doran A, Beavers CM, Treger A, Williams Q, MacDowell AA (2018) Implementation and application of the peak scaling method for temperature measurement in the laser heated diamond anvil cell. Rev Sci Instrum 89:083903. https://doi.org/10.1063/1.5028276

Kupenko I, Dubrovinsky L, Dubrovinskaia N, McCammon C, Glazyrin K, Bykova E, Ballaran TB, Sinmyo R, Chumakov AI, Potapkin V (2012) Portable double-sided laser-heating system for Mössbauer spectroscopy and X-ray diffraction experiments at synchrotron facilities with diamond anvil cells. Rev Sci Instrum 83:124501–1-124501–6. https://doi.org/10.1063/1.4772458

Laasch R, Liu Z, Ma L, Nicholas S, Northrup P, Thieme J, Whitaker ML (2022) From outer space to the center of the Earth: how NSLS-II capabilities enable geoscience studies. Synchrotron Radiat News 35:2–7. https://doi.org/10.1080/08940886.2022.2156752

Lavina B, Dera P, Downs RT (2014) Modern X-ray diffraction methods in mineralogy and geosciences. Rev Mineral Geochem 78:1–31

Liermann H-P, Merkel S, Miyagi L, Wenk H-R, Shen G, Cynn H, Evans WJ (2009) Experimental method for in situ determination of material textures at simultaneous high pressure and high temperature by means of radial diffraction in the diamond anvil cell. Rev Sci Instrum 80:104501. https://doi.org/10.1063/1.3236365

Loutherback K, Birarda G, Chen L, Holman NH-Y (2016) Microfluidic approaches to synchrotron radiation-based Fourier transform infrared (SR-FTIR) spectral microscopy of living biosystems. Protein Pept Lett 23:273–282. https://doi.org/10.2174/0929866526366160106154035

Lu Y-H, Larson JM, Baskin A, Zhao X, Ashby PD, Prendergast D, Bechtel HA, Kostecki R, Salmeron M (2019) Infrared nanospectroscopy at the graphene–electrolyte interface. Nano Lett 19:5388–5393. https://doi.org/10.1021/acs.nanolett.9b01897

Lutterotti L, Matthies S, Wenk H (1999) MAUD: a friendly Java program for material analysis using diffraction. CPD NEWSLETTER 21:14–15

Mao H-k, Shu J, Fei Y, Hu J, Hemley RJ (1996) The wüstite enigma. Phys Earth Planet Inter 96:135–145. https://doi.org/10.1016/0031-9201(96)03146-9

Merkel S (2006) X-ray diffraction evaluation of stress in high pressure deformation experiments. J Phys Condens Matter 18:S949. https://doi.org/10.1088/0953-8984/18/25/S03

Merkel S, Yagi T (2005) X-ray transparent gasket for diamond anvil cell high pressure experiments. Rev Sci Instrum 76:046109. https://doi.org/10.1063/1.1884195

Merkel S, Wenk H-R, Gillet P, Mao H-k, Hemley RJ (2004) Deformation of polycrystalline iron up to 30 GPa and 1000 K. Phys Earth Planet Inter 145:239–251. https://doi.org/10.1016/j.pepi.2004.04.001

Merkel S, Liermann H-P, Miyagi L, Wenk H-R (2013) In situ radial X-ray diffraction study of texture and stress during phase transformations in bcc-, fcc-and hcp-iron up to 36 GPa and 1000 K. Acta Mater 61:5144–5151. https://doi.org/10.1016/j.actamat.2013.04.068

Miyagi L, Wenk H-R (2016) Texture development and slip systems in bridgmanite and bridgmanite+ ferropericlase aggregates. Phys Chem Miner 43:597–613. https://doi.org/10.1007/s00269-016-0820-y

Miyagi L, Kunz M, Knight J, Nasiatka J, Voltolini M, Wenk H-R (2008) In situ phase transformation and deformation of iron at high pressure and temperature. J Appl Phys 104:103510. https://doi.org/10.1063/1.3008035

Miyagi L, Kanitpanyacharoen W, Kaercher P, Lee KK, Wenk H-R (2010) Slip systems in $MgSiO_3$ post-perovskite: implications for D″ anisotropy. Science 329:1639–1641. https://doi.org/10.1126/science.1192465

Miyagi L, Kanitpanyacharoen W, Raju SV, Kaercher P, Knight J, MacDowell A, Wenk H-R, Williams Q, Alarcon EZ (2013) Combined resistive and laser heating technique for in situ radial X-ray diffraction in the diamond anvil cell at high pressure and temperature. Rev Sci Instrum 84:025118. https://doi.org/10.1063/1.4793398

Nichols JB, Voltolini M, Gilbert B, MacDowell AA, Czabaj MW (2022) The hard X-ray nanotomography microscope at the advanced light source. Rev Sci Instrum 93:023704. https://doi.org/10.1063/5.0076322

Nisr C, Chen H, Leinenweber K, Chizmeshya A, Prakapenka VB, Prescher C, Tkachev SN, Meng Y, Liu Z, Shim S-H (2020) Large H_2O solubility in dense silica and its implications for the interiors of water-rich planets. Proc Natl Acad Sci 117:9747–9754. https://doi.org/10.1073/pnas.1917448117

Poirier J-P (2000) Introduction to the physics of the Earth's interior. Cambridge University Press, Cambridge

Prescher C, Prakapenka VB (2015) DIOPTAS: a program for reduction of two-dimensional X-ray diffraction data and data exploration. High Press Res 35:223–230

Probst AJ, Holman H-YN, DeSantis TZ, Andersen GL, Birarda G, Bechtel HA, Piceno YM, Sonnleitner M, Venkateswaran K, Moissl-Eichinger C (2013) Tackling the minority: sulfate-reducing bacteria in an archaea-dominated subsurface biofilm. ISME J 7:635–651

Quartieri S (2015) Synchrotron radiation in the earth sciences. In: Mobilio S, Boscherini F, Meneghini C (eds) Synchrotron radiation: basics, methods and applications. Springer, Berlin, pp 641–660

Rainey E, Kavner A (2014) Peak scaling method to measure temperatures in the laser-heated diamond anvil cell and application to the thermal conductivity of MgO. J Geophys Res Solid Earth 119:8154–8170

Raju S, Godwal B, Singh A, Jeanloz R, Saxena S (2018) High-pressure strengths of Ni_3Al and Ni–Al–Cr. J Alloy Compd 741:642–647

Ringwood AE (1991) Phase transformations and their bearing on the constitution and dynamics of the mantle. Geochim Cosmochim Acta 55:2083–2110

Rivers M, Prakapenka VB, Kubo A, Pullins C, Holl CM, Jacobsen SD (2008) The COMPRES/GSECARS gas-loading system for diamond anvil cells at the Advanced Photon Source. High Press Research 28:273–292

Rybacki E, Janssen C, Wirth R, Chen K, Wenk H-R, Stromeyer D, Dresen G (2011) Low-temperature deformation in calcite veins of SAFOD core samples (San Andreas Fault)—microstructural analysis and implications for fault rheology. Tectonophysics 509:107–119

Sakai T, Ohtani E, Terasaki H, Sawada N, Kobayashi Y, Miyahara M, Nishijima M, Hirao N, Ohishi Y, Kikegawa T (2009) Fe–Mg partitioning between perovskite and ferropericlase in the lower mantle. Am Miner 94:921–925

Sandford SA, Aléon J, Alexander CMOD, Araki T, Sa B, Baratta GA, Borg J, Bradley JP, Brownlee DE, Brucato JR (2006) Organics captured from comet 81P/Wild 2 by the Stardust spacecraft. Science 314:1720–1724

Speziale S, Immoor J, Ermakov A, Merkel S, Marquardt H, Liermann H-P (2019) The equation of state of TaC0. 99 by X-ray

diffraction in radial scattering geometry to 32 GPa and 1073 K. J Appl Phys 126:105107
Stan CV, Beavers CM, Kunz M, Tamura N (2018) X-ray diffraction under extreme conditions at the Advanced Light Source. Quantum Beam Sci 2:4
Stoe C (2009) X-Area V1. 76 Software. Stoe & Cie GmbH, Darmstadt, Germany Software
Sutton SR, Rivers ML, Smith JV, Brown GE Jr, Jones KW (1988) Synchrotron X ray sources in the Earth sciences. EOS Trans Am Geophys Union 69:1666–1675
Sutton S, Rivers M, Chariton S, Eng P, Lanzirotti A, Newville M, Officer T, Prakapenka V, Ryu Y, Stubbs J (2022) GeoSoilEnviroCARS (Sector 13) at the Advanced Photon Source: a comprehensive synchrotron radiation facility for Earth science research at ambient and extreme conditions. Phys Chem Miner 49:32
Tamura N, MacDowell A, Spolenak R, Valek B, Bravman J, Brown W, Celestre R, Padmore H, Batterman B, Patel J (2003) Scanning X-ray microdiffraction with submicrometer white beam for strain/stress and orientation mapping in thin films. J Synchrotron Radiat 10:137–143
Tschauner O, Huang S, Greenberg E, Prakapenka V, Ma C, Rossman G, Shen A, Zhang D, Newville M, Lanzirotti A (2018) Ice-VII inclusions in diamonds: evidence for aqueous fluid in Earth's deep mantle. Science 359:1136–1139
Tschauner O, Huang S, Yang S, Humayun M, Liu W, Gilbert Corder SN, Bechtel HA, Tischler J, Rossman GR (2021) Discovery of davemaoite, $CaSiO_3$-perovskite, as a mineral from the lower mantle. Science 374:891–894
Valek B, Bravman J, Tamura N, MacDowell A, Celestre R, Padmore H, Spolenak R, Brown W, Batterman B, Patel J (2002) Electromigration-induced plastic deformation in passivated metal lines. Appl Phys Lett 81:4168–4170
Voltolini M (2021) In-situ 4D visualization and analysis of temperature-driven creep in an oil shale propped fracture. J Petrol Sci Eng 200:108375
Voltolini M, Ajo-Franklin J (2019) The effect of CO_2-induced dissolution on flow properties in Indiana Limestone: an in situ synchrotron X-ray micro-tomography study. Int J Greenhouse Gas Control 82:38–47
Voltolini M, Ajo-Franklin JB (2020) The sealing mechanisms of a fracture in opalinus clay as revealed by in situ synchrotron X-ray micro-tomography. Front Earth Sci 8:207
Voltolini M, Barnard H, Creux P, Ajo-Franklin J (2019) A new mini-triaxial cell for combined high-pressure and high-temperature in situ synchrotron X-ray microtomography experiments up to 400 C and 24 MPa. J Synchrotron Radiat 26:238–243
Wenk H-R, Matthies S, Donovan J, Chateigner D (1998) BEARTEX: a Windows-based program system for quantitative texture analysis. J Appl Crystallogr 31:262–269
Wenk H, Lonardelli I, Merkel S, Miyagi L, Pehl J, Speziale S, Tommaseo C (2006) Deformation textures produced in diamond anvil experiments, analysed in radial diffraction geometry. J Phys Condens Matter 18:S933
Wenk H-R, Chandler BC, Chen K, Li Y, Tamura N, Yu R (2020) Residual lattice strain in quartzites as a potential palaeo-piezometer. Geophys J Int 222:1363–1378
Westphal AJ, Stroud RM, Bechtel HA, Brenker FE, Butterworth AL, Flynn GJ, Frank DR, Gainsforth Z, Hillier JK, Postberg F (2014) Evidence for interstellar origin of seven dust particles collected by the Stardust spacecraft. Science 345:786–791
Whittaker S, Thorne MS, Schmerr NC, Miyagi L (2016) Seismic array constraints on the D″discontinuity beneath Central America. J Geophys Res Solid Earth 121:152–169
Wicks J, Jackson J, Sturhahn W (2010) Very low sound velocities in iron-rich (Mg, Fe) O: implications for the core-mantle boundary region. Geophys Res Lett 37:L15304–1–L15304–5
Wong-Ng W, Siegrist T, DeTitta G, Finger L, Evans H Jr, Gabe E, Enright G, Armstrong J, Levenson M, Cook LP (2001) Standard reference material (SRM 1990) for single crystal diffractometer alignment. J Res Nat Inst Stand Technol 106:1071
Yagi T (1988) MAX80: Large-volume high-pressure apparatus combined with synchrotron radiation. EOS Trans Am Geophys Union 69:18–27
Yen CE, Williams Q, Kunz M (2020) Thermal pressure in the laser-heated diamond anvil cell: a quantitative study and implications for the density versus mineralogy correlation of the mantle. J Geophys Res Solid Earth 125:e2020JB020006
Young J, Glotch TD, Yesiltas M, Hamilton VE, Breitenfeld LB, Bechtel HA, Corder SG, Yao Z (2022) Nano-FTIR investigation of the CM chondrite allan hills 83100. J Geophys Res Planets 127:e2021JE007166
Yue B, Hong F, Hirao N, Vasin R, Wenk H-R, Chen B, Mao H-K (2019) A simple variant selection in stress-driven martensitic transformation. Proc Natl Acad Sci 116:14905–14909
Zhang D, Xu J, Dera PK, Rivers ML, Eng PJ, Prakapenka VB, Stubbs JE (2022) Recent developments on high-pressure single-crystal X-ray diffraction at the Partnership for eXtreme Xtallography (PX2) program. Phys Chem Miner 49:19
Zhao X, Li D, Lu Y-H, Rad B, Yan C, Bechtel HA, Ashby PD, Salmeron MB (2022) In vitro investigation of protein assembly by combined microscopy and infrared spectroscopy at the nanometer scale. Proc Natl Acad Sci 119:e2200019119
Zhou X, Tamura N, Mi Z, Lei J, Yan J, Zhang L, Deng W, Ke F, Yue B, Chen B (2017) Reversal in the size dependence of grain rotation. Phys Rev Lett 118:096101
Zuo L, Ajo-Franklin JB, Voltolini M, Geller JT, Benson SM (2017) Pore-scale multiphase flow modeling and imaging of CO_2 exsolution in Sandstone. J Petrol Sci Eng 155:63–77

Publisher's Note Springer Nature remains neutral with regard to jurisdictional claims in published maps and institutional affiliations.